Electronic Supplementary Information (ESI) to accompany:

Methodologies for Evaluation of Metal-Organic Frameworks in Separation Applications

Rajamani Krishna

Van 't Hoff Institute for Molecular Sciences, University of Amsterdam, Science Park 904,

1098 XH Amsterdam, The Netherlands

CORRESPONDING AUTHOR *Tel +31 20 6270990; Fax: + 31 20 5255604;

email: r.krishna@contact.uva.nl

Table of Contents

1. Simulation methodology for transient breakthrough in fixed bed adsorbers

Fixed bed, packed with crystals of microporous materials, are commonly used for separation of mixtures (see schematic in Figure **2**); such adsorbers are commonly operated in a transient mode, and the compositions of the gas phase, and component loadings within the crystals, vary with position and time. During the initial stages of the transience, the pores are loaded up gradually, and only towards the end of the adsorption cycle are conditions corresponding to pore saturation attained. Put another way, separations in fixed bed adsorbers are influenced by both the Henry regime of adsorption as well as the conditions corresponding to pore saturation. Experimental data on the transient breakthrough of mixtures across fixed beds are commonly used to evaluate and compare the separation performance of zeolites and MOFs.[1-5] For a given separation task, transient breakthroughs provide more a realistic evaluation of the efficacy of a material, as they reflect the combined influence of adsorption selectivity, adsorption capacity, and intra-crystalline diffusion limitations.[5, 6]

We describe below the simulation methodology used to perform transient breakthrough calculations that are presented in this work. This simulation methodology is the same as that used in our previous published work.[5]

Assuming plug flow of an *n*-component gas mixture through a fixed bed maintained under isothermal conditions, the partial pressures in the gas phase at any position and instant of time are obtained by solving the following set of partial differential equations for each of the species *i* in the gas mixture.[7]

$$\frac{1}{RT}\frac{\partial p_i(t,z)}{\partial t} = -\frac{1}{RT}\frac{\partial\left(v(t,z)p_i(t,z)\right)}{\partial z} - \frac{\left(1-\varepsilon\right)}{\varepsilon}\rho\frac{\partial \bar{q}_i(t,z)}{\partial t}; \quad i = 1,2,...n \tag{1}$$

In equation (1), t is the time, z is the distance along the adsorber, ρ is the framework density, ε is the bed voidage, v is the interstitial gas velocity, and $\bar{q}_i(t,z)$ is the *spatially averaged* molar loading within the crystallites of radius r_c, monitored at position z, and at time t.

At any time t, during the transient approach to thermodynamic equilibrium, the spatially averaged molar loading within the crystallite r_c is obtained by integration of the radial loading profile

$$\bar{q}_i(t) = \frac{3}{r_c^3}\int_0^{r_c} q_i(r,t) r^2 dr \tag{2}$$

For transient unary uptake within a crystal at any position and time with the fixed bed, the radial distribution of molar loadings, q_i, within a spherical crystallite, of radius r_c, is obtained from a solution of a set of differential equations describing the uptake

$$\frac{\partial q_i(r,t)}{\partial t} = -\frac{1}{\rho}\frac{1}{r^2}\frac{\partial}{\partial r}\left(r^2 N_i\right) \tag{3}$$

The molar flux N_i of component i is described by the simplified version of the Maxwell-Stefan equations in which both correlation effects and thermodynamic coupling effects are considered to be of negligible importance[5]

$$N_i = -\rho Đ_i \frac{\partial q_i}{\partial r} \tag{4}$$

Summing equation (**2**) over all n species in the mixture allows calculation of the *total average* molar loading of the mixture within the crystallite

$$\bar{q}_t(t,z) = \sum_{i=1}^{n} \bar{q}_i(t,z) \tag{5}$$

The *interstitial* gas velocity is related to the *superficial* gas velocity by

$$v = \frac{u}{\varepsilon} \tag{6}$$

In industrial practice, the most common operation is with to use a step-wise input of mixtures to be separation into an adsorber bed that is initially free of adsorbates, i.e. we have the initial condition

$$t = 0; \quad q_i(0,z) = 0 \tag{7}$$

At time, $t = 0$, the inlet to the adsorber, $z = 0$, is subjected to a step input of the n-component gas mixture and this step input is maintained till the end of the adsorption cycle when steady-state conditions are reached.

$$t \geq 0; \quad p_i(0,t) = p_{i0}; \quad u(0,t) = u \tag{8}$$

where u is the superficial gas velocity at the inlet to the adsorber.

Besides, the breakthrough simulations with a step-input (8), we also carried out simulations for a packed bed adsorber with injection of a short duration pulse of the mixture to be separated. This type of simulation is particularly useful to demonstrate the fractionating capability of adsorbents. For simulation of pulse chromatographic separations, we use the corresponding set of inlet conditions

$$0 \leq t \leq t_0; \quad p_i(0,t) = p_{i0}; \quad u(0,t) = u \tag{9}$$

where the time for duration of the pulse is t_0. The pulse duration is generally very short, and therefore pore saturation conditions are never approached at any position at any time t. Therefore, pulse chromatographic simulations, and the corresponding experiments, do not reflect molecular packing effects. Pulse chromatographic simulations and experiments are representative of separations in the Henry regime at low pore occupancies.[8, 9] Pulse chromatographic experiments have been used to demonstrate the potential of MOFs for separations at of alkane isomers,[10] and xylene isomers[11, 12] at low pore occupancies. In this review article, pulse chromatographic simulations are only used to demonstrate the separation of noble gases using CuBTC.

If the value of $\frac{Đ_i}{r_c^2}$ is large enough to ensure that intra-crystalline gradients are absent and the entire crystallite particle can be considered to be in thermodynamic equilibrium with the surrounding bulk gas phase at that time t, and position z of the adsorber

$$\bar{q}_i(t,z) = q_i(t,z) \tag{10}$$

The molar loadings at the *outer surface* of the crystallites, i.e. at $r = r_c$, are calculated on the basis of adsorption equilibrium with the bulk gas phase partial pressures p_i at that position z and time t. The

adsorption equilibrium can be calculated on the basis of the Ideal Adsorbed Solution Theory (IAST) of Myers and Prausnitz.[13] In all the simulation results we present in this article, the IAST calculations use pure component isotherms fitted with the Langmuir, Langmuir-Freundlich, or dual-Langmuir-Freundlich model.

For presenting the breakthrough simulation results, we use the dimensionless time, $\tau = \frac{tu}{L\varepsilon}$, obtained by dividing the actual time, t, by the characteristic time, $\frac{L\varepsilon}{u}$, where L is the length of adsorber, u is the superficial fluid velocity, ε is the bed voidage.[6]

For all the simulations reported in this article we choose the following: adsorber length, L = 0.3 m; cross-sectional area, A = 1 m^2; superficial gas velocity in the bed, u = 0.04 m s^{-1}; voidage of the packed bed, ε = 0.4. Please note that since the superficial gas velocity is specified, the specification of the cross-sectional area of the tube, A, is not relevant in the simulation results presented. The volume of MOF used in the simulations is (1 - ε) A L = 0.18 m^3. If ρ is the framework density, the mass of the adsorbent in the bed is ρ (1 - ε) A L kg. In these breakthrough simulations we use the same volume of adsorbent in the breakthrough apparatus, i.e. (1 - ε) A L = 0.18 m^3.

2. Transient breakthrough experiments for CO_2/CH_4 separations

We analyze a set of experimental breakthroughs for 50/50 CO_2/CH_4 mixtures in bed packed with NiMOF-74 and Kureha carbon measured in the same set-up and reported by Chen et al.[14] and Yu et al.[15] The tube length, L =100 mm and the internal diameter, d = 4.65 mm; see schematic in Figure **2**.

The cross-sectional area of the tube, is

$$A = \frac{\pi}{4} d^2 \tag{11}$$

The volume of the empty tube, V, is

$$V = AL \tag{12}$$

Let m_{ads} represent the mass of adsorbent packed into the tube. The volume occupied by the adsorbent crystalline material, V_{ads}, is

$$V_{ads} = \frac{m_{ads}}{\rho} \tag{13}$$

A precisely determined mass of each adsorbent (Ni-MOF-74 pellet sample = 576.1 mg, and Kureha carbon = 760 mg) was filled into the column and then heated in flowing He with a rate of 20 ml (STP) min^{-1} at 423 K for 8 h prior to the breakthrough measurements. The breakthrough curves were then measured by switching the He flow to a flow containing CO_2 and CH_4 in He (used as a balance) with a CO_2:CH_4:He mole composition of 1:1:2 at a total flow rate of 8 mL (STP) min^{-1}.

As illustration, Figures 3a,b compares the experimental breakthroughs for CO_2(1)/CH_4(2)/He(3) in packed bed with NiMOF-74, and Kureha carbon at 298 K. The partial pressures at the inlet are $p_1 = p_2 =$ 50 kPa; $p_3 = 100$ kPa. For both materials, with the notable exception of NH_2-MIL-101, there is a finite time interval within which 99%+ pure CH_4 can be produced. As illustration in Figure 3b, for NiMOF-74 it is possible to produce CH_4 with 99%+ purity during the time interval between t_1, and t_2.

The gravimetric CO_2 uptake can be calculated from

$$\text{CO}_2 \text{ uptake} = \frac{c_t Q_{He}}{m_{ads}} \int_0^{t_{ss}} \left(\frac{y_{CO2,inlet}}{y_{He,inlet}} - \frac{y_{CO2,exit}}{y_{He,exit}} \right) dt - \frac{\left(c_t y_{CO2,exit}\right)}{m_{ads}} \left(AL - V_{ads}\right) \tag{14}$$

The volumetric CO_2 uptake is obtained by multiplying by the framework density (= grain density) of the adsorbent. Figure 3c shows the dependence of the volumetric uptake on the dimensionless breakthrough time.

A material balance for the time interval $t = t_1 - t_2$ allows us to determine the productivity of CH_4 with the specified 99%+ purity

$$\text{CH}_4 \text{ productivity} = \frac{c_t Q_{He}}{m_{ads}} \int_{t_1}^{t_2} \left(\frac{y_{CH4,exit}}{y_{He,exit}} \right) dt \tag{15}$$

3. C_2H_2/CO_2 separations

MOF	Surface area $m^2\ g^{-1}$	Pore volume $cm^3\ g^{-1}$	Framework density $kg\ m^{-3}$	Data sources for unary isotherm fits	Comment
HOF-3	165	0.0971	453	[16]	
ZJU-60a	1627	0.868	631	[17]	
CuBTC	2097	0.848	879	[18, 19]	
PCP-33	1248	0.502	1261	[20]	
Cu_2TPTC	2405		760	[21]	

HOF-3 is a rod-packing 3D microporous hydrogen-bonded organic framework exhibiting the **srs** topology.[16]

ZJU-60a = Cu_2(MFDI) is a three-dimensional microporous metal–organic framework with a rare **sty-a** type topology.[17]

CuBTC (=$Cu_3(BTC)_2$ with BTC = 1,3,5-benzenetricarboxylate, also known as HKUST-1) structure consists of two types of "cages" and two types of "windows" separating these cages. Large cages are inter-connected by 9 Å windows of square cross-section. The large cages are also connected to tetrahedral-shaped pockets of ca. 6 Å size through triangular-shaped windows of ca. 4.6 Å size.

PCP-33 = $[(Cu_4Cl)(BTBA)_8\cdot(CH_3)_2NH_2)]$ based on a symmetric ligand (3,5-bis(2H-tetrazol-5-yl)-benzoic acid, H_3BTBA).[20]

Cu_2TPTC-Me (TPTC-Me =2′,5′-dimethyl-[1,1′:4′,1″-terphenyl]-3,3″,5,5″-tetracarboxylate) is a NbO type isostructural MOF synthesized by Xia et al. [21]. The separation performance of this MOF is almost identical to that of PCP-33. The comparison of the C_2H_2/CO_2 mixture separations using Cu_2TPTC-Me with the four other MOFs are provided in Figure 4.

Figures 4a, 4b show IAST calculations of (a) adsorption selectivity, S_{ads}, and (b) uptake capacity of C_2H_2, for separation of 50/50 C_2H_2/CO_2 mixture.

Figure 4c compares the % C_2H_2 in the exit gas plotted as a function of the dimensionless breakthrough time. We see that the breakthrough time for Cu_2TPTC-Me is identical to that of PCP-33.

4. Xe/Kr separations

MOF	Surface area $m^2\ g^{-1}$	Pore volume $cm^3\ g^{-1}$	Framework density $kg\ m^{-3}$	Data sources for unary isotherm fits	Comment
Ag@NiMOF-74	750		1240	[22]	Intra-crystalline diffusion effects are not significant
NiMOF-74	1532	0.582	1220	[22, 23]	
CuBTC	2097	0.848	879	[23, 24]	
SBMOF-2			1192	[25]	
CoFormate	300		1819	[26]	Intra-crystalline diffusion effects are not significant

NiMOF-74 = (Ni_2 (dobdc) = Ni\(dobdc) with dobdc = (dobdc4– = 1,4-dioxido-2,5-benzenedicarboxylate)). This MOF consists of one-dimensional hexagonal-shaped channels with free internal diameter of ca. 11 Å.

Ag@NiMOF-74 = silver loaded NiMOF-74.[22]

CuBTC (=$Cu_3(BTC)_2$ with BTC = 1,3,5-benzenetricarboxylate, also known as HKUST-1) structure consists of two types of "cages" and two types of "windows" separating these cages. Large cages are inter-connected by 9 Å windows of square cross-section. The large cages are also connected to tetrahedral-shaped pockets of ca. 6 Å size through triangular-shaped windows of ca. 4.6 Å size.

SBMOF-2 (Stony Brook MOF-2) is a robust 3-D porous crystalline structure containing calcium and 1,2,4,5-tetrakis(4-carboxyphenyl)benzene. [26]

CoFormate = $Co_3(HCOO)_6$. The framework contains one-dimensional channels made of repeating zig and zag segment running along the crystallographic *b*-axis, of which the pore diameter is about 5 Å.

5. CO_2/N_2 separations

MOF	Surface area $m^2\ g^{-1}$	Pore volume $cm^3\ g^{-1}$	Framework density $kg\ m^{-3}$	Data sources for unary isotherm fits	Comment
MgMOF-74	1669	0.607	909	[19, 27]	Intra-crystalline diffusion effects are not significant
NiMOF-74	1532	0.582	1194	[28, 29]	
NaX	950	0.280	1421	[19, 30]	
Kureha carbon	1300	0.56	1860	[15]	
Cu-SSZ13		0.253	1852	[31, 32]	Intra-crystalline diffusion effects are significant

MgMOF-74 (= Mg_2 (dobdc) = Mg\(dobdc) with dobdc = (dobdc4– = 1,4-dioxido-2,5-benzenedicarboxylate)), This MOF consists of one-dimensional hexagonal-shaped channels with free internal diameter of ca. 11 Å

NiMOF-74 = (Ni_2 (dobdc) = Ni\(dobdc) with dobdc = (dobdc4– = 1,4-dioxido-2,5-benzenedicarboxylate)). This MOF consists of one-dimensional hexagonal-shaped channels with free internal diameter of ca. 11 Å

NaX zeolite, also referred to as 13 X zeolite, has the FAU topology. The FAU topology consists of 785.7 $Å^3$ size cages separated by 7.4 Å size windows. Cage size is calculated on the basis of the equivalent sphere volume.

Kureha carbon is a commercially available, purely microporous material with pore-size distribution centered at 0.6 and 1.1 nm.[15]

Cu-SSZ13 has the CHA zeolite topology. CHA topology consists of 316.4 $Å^3$ size cages separated by 3.77 Å × 4.23 Å size windows.

6. $CO_2/N_2/SO_2$ separations

MOF	Surface area $m^2\ g^{-1}$	Pore volume $cm^3\ g^{-1}$	Framework density $kg\ m^{-3}$	Data sources for unary isotherm fits	Comment
NOTT-300	1370	0.433	1062	[33]	

NOTT-300 = $[Al_2(OH)_2(C_{16}O_8H_6)]$.[33] The pore dimensions are 6.5 Å × 6.5 Å.

7. CO_2/CH_4 separations

MOF	Surface area $m^2\ g^{-1}$	Pore volume $cm^3\ g^{-1}$	Framework density $kg\ m^{-3}$	Data sources for unary isotherm fits	Comment
MgMOF-74	1669	0.607	909	[19, 27]	Intra-crystalline diffusion effects are not significant
NiMOF-74	1532	0.582	1194	[28, 29]	
NaX	950	0.280	1421	[19, 30]	
CuBTC	2097	0.848	879	[19, 34]	
Cu-TDPAT	1938	0.93	782	[19, 35]	
Kureha carbon	1300	0.56	1860	[15]	

MgMOF-74 (= Mg_2 (dobdc) = Mg\(dobdc) with dobdc = (dobdc4– = 1,4-dioxido-2,5-benzenedicarboxylate)). This MOF consists of one-dimensional hexagonal-shaped channels with free internal diameter of ca. 11 Å

NiMOF-74 = (Ni_2 (dobdc) = Ni\(dobdc) with dobdc = (dobdc4– = 1,4-dioxido-2,5-benzenedicarboxylate)). This MOF consists of one-dimensional hexagonal-shaped channels with free internal diameter of ca. 11 Å

NaX zeolite, also referred to as 13 X zeolite, has the FAU topology. The FAU topology consists of 785.7 $Å^3$ size cages separated by 7.4 Å size windows. Cage size is calculated on the basis of the equivalent sphere volume.

CuBTC (=$Cu_3(BTC)_2$ with BTC = 1,3,5-benzenetricarboxylate, also known as HKUST-1) structure consists of two types of "cages" and two types of "windows" separating these cages. Large cages are inter-connected by 9 Å windows of square cross-section. The large cages are also connected to tetrahedral-shaped pockets of ca. 6 Å size through triangular-shaped windows of ca. 4.6 Å size

Cu-TDPAT =an rht-type metal−organic framework; H_6TDPAT = 2,4,6-tris(3,5-dicarboxylphenylamino)-1,3,5-triazine.

Kureha carbon is a commercially available, purely microporous material ,with pore-size distribution centered at 0.6 and 1.1 nm.[15]

The main manuscript compares separations at total pressures of 100 kPa and 2 MPa. Here, we also include comparisons with transient breakthroughs 600 kPa. Figure 5 presents a comparison of % CO_2 in the exit gas for fixed bed adsorber beds packed with different adsorbents, fed with 50/50 CO_2/CH_4 mixture, operating at 298 K and (a) p_t = 100 kPa, (b) p_t = 600 kPa, (c) p_t = 2 MPa. Figure 6 presents plots of the amount of CO_2 captured during the time interval 0 - τ_{break} as function of the dimensionless breakthrough time, τ_{break}, for fixed bed adsorber beds packed with different adsorbents, fed with 50/50 CO_2/CH_4 mixture, operating at 298 K and (a) p_t = 100 kPa, (b) p_t = 600 kPa, (c) p_t = 2 MPa. (c) 100 kPa, and (b) 2 MPa.

8. $CO_2/CH_4/H_2S$ separations

MOF	Surface area $m^2\ g^{-1}$	Pore volume $cm^3\ g^{-1}$	Framework density $kg\ m^{-3}$	Data sources for unary isotherm fits	Comment
NiMOF-74	1532	0.582	1194	[28, 29, 36]	Intra-crystalline diffusion effects are not significant
Amino-MIL-125 (Ti)	950	0.280	1421	[37]	

NiMOF-74 = (Ni_2 (dobdc) = Ni\(dobdc) with dobdc = (dobdc4– = 1,4-dioxido-2,5-benzenedicarboxylate)). This MOF consists of one-dimensional hexagonal-shaped channels with free internal diameter of ca. 11 Å.

Amino-MIL-125 (Ti) = MIL-125(Ti)-NH_2 = amino functionalized titanium terephthalate. MIL-125(Ti)-NH_2 exhibits a quasi-cubic tetragonal structure. The octahedral and tetrahedral cages with calculated free diameters of 10.7 Å and 4.7 Å are accessible through triangular windows of 5–7 Å.[37]

9. Separation of H_2 from $H_2/CO_2/CO/CH_4/N_2$ mixtures

MOF	Surface area $m^2\ g^{-1}$	Pore volume $cm^3\ g^{-1}$	Framework density $kg\ m^{-3}$	Data sources for unary isotherm fits	Comment
UTSA-16a extrudates	805	0.49	1171	The isotherm data used are from Agueda et al.[38]	Intra-crystalline diffusion effects are not significant
Cu-TDPAT	1938	0.93	782	[19, 35]	
NaX zeolite	950	0.280	1421	[19, 30]	
CuBTC	2097	0.848	879	[19, 39]	
Activated Carbon (AC)			1000	[40]	

The simulation details are provided in our earlier work. [5]

Cu-TDPAT =an rht-type metal−organic framework; H_6TDPAT = 2,4,6-tris(3,5-dicarboxylphenylamino)-1,3,5-triazine.

NaX zeolite, also referred to as 13 X zeolite, has the FAU topology. The FAU topology consists of 785.7 $Å^3$ size cages separated by 7.4 Å size windows. Cage size is calculated on the basis of the equivalent sphere volume.

CuBTC (=$Cu_3(BTC)_2$ with BTC = 1,3,5-benzenetricarboxylate, also known as HKUST-1) structure consists of two types of "cages" and two types of "windows" separating these cages. Large cages are inter-connected by 9 Å windows of square cross-section. The large cages are also connected to tetrahedral-shaped pockets of ca. 6 Å size through triangular-shaped windows of ca. 4.6 Å size.

The isotherm data for Activated Carbon are taken from Banu et al. [40]

Experimental confirmation that intra-crystalline diffusion effects are not of significant importance for H_2 purification processes is obtained by an analysis of the experimental data of Silva et al.[41] on the breakthrough characteristics of 3-component 35.5/47/17.5 $H_2/CO_2/CH_4$ mixture in adsorber packed with CuBTC at 303 K operating at a total pressure of 0.2 MPa; see Figure 7. The experimental data (symbols) are compared with breakthrough simulations (continuous solid lines) assuming thermodynamic equilibrium, i.e. invoking Equation (10); the agreement is very good. Silva et al.[41] also present a detailed model for breakthrough that include: intra-crystalline diffusion, axial dispersion in the fixed bed, along with a rigorous energy balance. Their simulation results, presented in Figure 4a of their paper, are hardly distinguishable from our own simulations using invoking Equation (10) that assumes thermodynamic equilibrium.

10. Fuel-cell grade H_2 production from $H_2/CO_2/CO$ mixtures

MOF	Surface area $m^2\ g^{-1}$	Pore volume $cm^3\ g^{-1}$	Framework density $kg\ m^{-3}$	Data sources for unary isotherm fits	Comment
UTSA-16a extrudates	805	0.49	1171	The isotherm data used are from Agueda et al.[38]	Intra-crystalline diffusion effects are not significant
Cu-TDPAT	1938	0.93	782	[19, 35]	
NaX zeolite	950	0.280	1421	[19, 30]	
CuBTC	2097	0.848	879	[19, 39]	
Activated Carbon (AC)			1000	[40]	

The simulation details are provided in our earlier work. [5]

Cu-TDPAT =an rht-type metal−organic framework; H_6TDPAT = 2,4,6-tris(3,5-dicarboxylphenylamino)-1,3,5-triazine.

NaX zeolite, also referred to as 13 X zeolite, has the FAU topology. The FAU topology consists of 785.7 $Å^3$ size cages separated by 7.4 Å size windows. Cage size is calculated on the basis of the equivalent sphere volume.

CuBTC (=$Cu_3(BTC)_2$ with BTC = 1,3,5-benzenetricarboxylate, also known as HKUST-1) structure consists of two types of "cages" and two types of "windows" separating these cages. Large cages are inter-connected by 9 Å windows of square cross-section. The large cages are also connected to tetrahedral-shaped pockets of ca. 6 Å size through triangular-shaped windows of ca. 4.6 Å size.

The isotherm data for Activated Carbon are taken from Banu et al. [40]

Figure 8a plots the ppm impurities in outlet gas as a function of the dimensionless time for separation of 3-component 73/16/11 $H_2/CO_2/CO$ mixtures. We aim for impurity levels < 10 ppm. [42]

Figure 8b compares the plots of the amount of H_2 captured (< 10 ppm impurities) per L of material during the time interval 0 - τ_{break} as function of the dimensionless breakthrough time, τ_{break} for separation of 3-component 73/16/11 $H_2/CO_2/CO$ mixtures. We note that NaX is the best adsorbent for production of fuel-cell grade hydrogen.

11. CO_2/CO mixture separations

MOF	Surface area $m^2\ g^{-1}$	Pore volume $cm^3\ g^{-1}$	Framework density $kg\ m^{-3}$	Data sources for unary isotherm fits	Comment
UTSA-16a extrudates	805	0.49	1171	The isotherm data used are from Agueda et al.[38]	Intra-crystalline diffusion effects are not significant
Cu-TDPAT	1938	0.93	782	[19, 35]	
NaX zeolite	950	0.280	1421	[19, 30]	
CuBTC	2097	0.848	879	[19, 39]	
Activated Carbon (AC)			1000	[40]	

The simulation details are provided in our earlier work. [5]

Cu-TDPAT =an rht-type metal−organic framework; H_6TDPAT = 2,4,6-tris(3,5-dicarboxylphenylamino)-1,3,5-triazine.

NaX zeolite, also referred to as 13 X zeolite, has the FAU topology. The FAU topology consists of 785.7 $Å^3$ size cages separated by 7.4 Å size windows. Cage size is calculated on the basis of the equivalent sphere volume.

CuBTC (=$Cu_3(BTC)_2$ with BTC = 1,3,5-benzenetricarboxylate, also known as HKUST-1) structure consists of two types of "cages" and two types of "windows" separating these cages. Large cages are inter-connected by 9 Å windows of square cross-section. The large cages are also connected to tetrahedral-shaped pockets of ca. 6 Å size through triangular-shaped windows of ca. 4.6 Å size.

The isotherm data for Activated Carbon are taken from Banu et al. [40]

Figure 9a presents a plot of ppm CO_2 in outlet gas as a function of the dimensionless time for separation of binary 50/50 CO_2/CO mixtures using five different adsorbent materials. CuBTC, NaX, Cu-TDPAT have nearly the same breakthrough times, that are significantly higher than that with UTSA-16a, and AC.

Figure 9b presents a plot of the amount of CO_2 captured per L of material during the time interval 0 - τ_{break} as function of the dimensionless breakthrough time, τ_{break}. NaX, CuBTC, and Cu-TDPAT have nearly the same CO_2 capture capabilities. The poorest CO_2 capture capability is that of AC.

12. C_2H_2/C_2H_4 separations at 298 K

MOF	Surface area $m^2\ g^{-1}$	Pore volume $cm^3\ g^{-1}$	Framework density $kg\ m^{-3}$	Data sources for unary isotherm fits	Comment
MgMOF-74	1669	0.607	909	[18]	Intra-crystalline diffusion effects are not significant
CoMOF-74	1448.5	0.515	1169	[18]	
FeMOF-74	1536	0.626	1126	[18]	
NOTT-300	1370	0.433	1062	The isotherm fits are from Table S13 of Yang.[43] The data is for 293 K.	
M'MOF3a	110	0.165	1023	[18]	
M'MOF4a		0.289	1126	[18]	
UTSA-100a	970	0.399	1146	[44]	

MgMOF-74 (= Mg_2 (dobdc) = Mg\(dobdc) with dobdc = (dobdc4– = 1,4-dioxido-2,5-benzenedicarboxylate)). This MOF consists of one-dimensional hexagonal-shaped channels with free internal diameter of ca. 11 Å

CoMOF-74 = (Co_2 (dobdc) = Co\(dobdc)) with dobdc = (dobdc4– = 1,4-dioxido-2,5-benzenedicarboxylate)). This MOF consists of one-dimensional hexagonal-shaped channels with free internal diameter of ca. 11 Å

FeMOF-74 (= Fe_2(dobdc) = Fe\(dobdc) with dobdc = (dobdc4– = 1,4-dioxido-2,5-benzenedicarboxylate)). This MOF consists of one-dimensional hexagonal-shaped channels with free internal diameter of ca. 11 Å

M'MOF3a = mixed metal organic-framework.[45] The pore dimensions are 3.4 Å × 4.8 Å

M'MOF4a = mixed metal organic-framework.[45]

NOTT-300 = $[Al_2(OH)_2(C_{16}O_8H_6)]$.[33] It has 6.5 Å × 6.5 Å channels.

UTSA-100a = a microporous MOF = [Cu(ATBDC)]; H_2ATBDC = 5-(5-Amino-1H-tetrazol-1-yl)-1,3-benzenedicarboxylic acid. [44] UTSA-100a has a three-dimensional framework with rhombic open zigzag nano-channels with amino and tetrazole functionalized wall running in the *c*-direction. The 1D open zigzag channels have a diameter of about 4.3 Å. There are smaller cages with the diameter of about 4.0 Å between the 1D channels with window openings of 3.3 Å.

The main manuscript examines 1/99 C_2H_2/C_2H_4 mixture separations. Figure 10 presents IAST, and breakthrough calculations for 50/50 C_2H_2/C_2H_4 mixtures using four different MOFs. We note that the highest capture capture capacity is achieved with MgMOF-74. These calculations demonstrate that uptake capacities are more important for 50.50 C_2H_2/C_2H_4 mixtures than for 1/99 C_2H_2/C_2H_4 mixtures.

13. C_2H_4/C_2H_6 and C_3H_6/C_3H_8 separations at 318 K

MOF	Surface area $m^2\ g^{-1}$	Pore volume $cm^3\ g^{-1}$	Framework density $kg\ m^{-3}$	Data sources for unary isotherm fits	Comment
MgMOF-74	1835	0.638	909	[46]	Intra-crystalline diffusion effects are not significant for thes MOFs
CoMOF-74	1438	0.51	1169	[46]	
FeMOF-74	1536	0.529	1126	[1, 46]	
NiMOF-74	1532	0.541	1206	[46]	
MnMOF-74	1797	0.628	1084	[46]	
ZnMOF-74	1277	0.451	1231	[46]	

The values above are reproduced from Tables S1 and S15 of Geier et al.[46]

Our simulations are carried out with the dual-Langmuir-Freundlich fit parameters in Tables S2, S3, S4, S5, S6, S7, S8, S9, S10, S11, S12, and S13.

MgMOF-74 (= Mg_2 (dobdc) = Mg\(dobdc) with dobdc = (dobdc4– = 1,4-dioxido-2,5-benzenedicarboxylate)). This MOF consists of one-dimensional hexagonal-shaped channels with free internal diameter of ca. 11 Å

CoMOF-74 = (Co_2 (dobdc) = Co\(dobdc)) with dobdc = (dobdc4– = 1,4-dioxido-2,5-benzenedicarboxylate)). This MOF consists of one-dimensional hexagonal-shaped channels with free internal diameter of ca. 11 Å

FeMOF-74 (= Fe_2(dobdc) = Fe\(dobdc) with dobdc = (dobdc4– = 1,4-dioxido-2,5-benzenedicarboxylate)). This MOF consists of one-dimensional hexagonal-shaped channels with free internal diameter of ca. 11 Å

NiMOF-74 = (Ni_2 (dobdc) = Ni\(dobdc) with dobdc = (dobdc4– = 1,4-dioxido-2,5-benzenedicarboxylate)). This MOF consists of one-dimensional hexagonal-shaped channels with free internal diameter of ca. 11 Å

MnMOF-74 (= Mn_2 (dobdc) = Mn\(dobdc)) with dobdc = (dobdc4– = 1,4-dioxido-2,5-benzenedicarboxylate)). This MOF consists of one-dimensional hexagonal-shaped channels with free internal diameter of ca. 11 Å

ZnMOF-74 (= Zn_2 (dobdc) = Zn\(dobdc)) with dobdc = (dobdc4– = 1,4-dioxido-2,5-benzenedicarboxylate)). This MOF consists of one-dimensional hexagonal-shaped channels with free internal diameter of ca. 11 Å.

Experimental data on the pure component isotherms for adsorption of C_2H_4,C_2H_6, C_3H_6, and C_3H_8 in six different iso-structural MOFs M-MOF-74 with M = Fe, Co, Ni, Zn, and Mn are available in the works of Bloch et al.[1], and Geier et al.[46] We shall use the pure component isotherm fits at 318 K to compare their relative performance for separations of 50/50 C_2H_4/C_2H_6, and 50/50 C_3H_6/C_3H_8 mixtures. The C_2H_4/C_2H_6 selectivities and volumetric C_2H_4 uptake capacities are compared in Figure 11a, and 11b. The highest selectivities are realized with FeMOF-74, and MnMOF-74. The higher volumetric uptake capacities are obtained with FeMOF-74, MnMOF-74, CoMOF-74, and NiMOF-74. Figures 11c presents a comparison of the % C_2H_4 in the exit gas from adsorber beds for the six different MOFs. Let us arbitrarily define the breakthrough time, τ_{break}, as the dimensionless time at which the % C_2H_4 in the exit gas is 1%. The longest breakthrough times, τ_{break}, are with FeMOF-74, MnMOF-74, CoMOF-74, and NiMOF-74; this appears to be dictated primarily the the hierarchy of volumetric uptake capacities. The shortest breakthrough times, τ_{break}, are with MgMOF-74 that has the lowest volumetric uptake capacity. The amount of C_2H_4 captured during the time interval 0 - τ_{break} can be determined from a material balance. These amounts, expressed as mol C_2H_4 captured per L of framework material are plotted against τ_{break} in Figures 11d. The highest capture C_2H_4 capacities are realized with FeMOF-74, MnMOF-74, CoMOF-74, and NiMOF-74 primarily because of high uptake capacities. By the same token, the lowest C_2H_4 capture capacity is realized with MgMOF-74 primarily because of its low volumetric uptake capacity.The C_3H_6/C_3H_8 selectivities and volumetric C_3H_6 uptake capacities are compared in Figures 12a, and 12b. The highest selectivities are realized with MnMOF-74, and FeMOF-74. The higher volumetric uptake capacities are obtained with NiMOF-74, FeMOF-74, and MnMOF-74. Figures 12c presents a comparison of the % C_3H_6 in the exit gas from adsorber beds for the six different MOFs. Let us arbitrarily define the breakthrough time, τ_{break}, as the dimensionless time at which the % C_3H_6 in the exit gas is 1%. The longest breakthrough times, τ_{break}, are with NiMOF-74,

FeMOF-74, and MnMOF-74; this appears to be dictated primarily the the hierarchy of volumetric uptake capacities. MgMOF-74, CoMOF-74, and FeMOF-74 primarily because of the higher uptake capacities. The shortest breakthrough times, τ_{break}, are with MgMOF-74 that has the lowest volumetric uptake capacity. The amount of C_3H_6 captured during the time interval 0 - τ_{break} can be determined from a material balance. These amounts, expressed as mol C_3H_6 captured per L of framework material are plotted against τ_{break} in Figures 12d. The highest capture C_3H_6 capacities are realized with NiMOF-74, FeMOF-74, and MnMOF-74 primarily because of high uptake capacities. By the same token, the lowest C_3H_6 capture capacity is realized with MgMOF-74 primarily because of its low volumetric uptake capacity.From the foregoing analyses of separation of C_2H_4/C_2H_6, and C_3H_6/C_3H_8 mixtures we conclude that M-MOF-74 have good potential for selective adsorption of unsaturated alkenes from mixtures with the corresponding saturated alkanes of the same chain length.

The energy requirements are high because of the significantly higher binding energy of the alkenes; this is reflected in the isosteric heats of adsorption; see Figure 13.

14. C_2H_4/C_2H_6 separations at 298 K

MOF	Surface area $m^2\ g^{-1}$	Pore volume $cm^3\ g^{-1}$	Framework density $kg\ m^{-3}$	Data sources for unary isotherm fits	Comment
MgMOF-74	1669	0.607	909	[18]	
CoMOF-74	1448.5	0.5146	1169	[18]	
FeMOF-74	1536	0.626	1126	[18]	
CuBTC	2097	0.848	879	[18]	
NOTT-300	1370	0.433	1062	The isotherm fits are from Table S13 of Yang.[43] The data is for 293 K.	
PAF-1-SO3Ag	1938	0.93	1070	[47]	
MIL-101-Cr-SO3Ag	1374	0.56	700	[48]	

Since the Geier et al. [46] data for MgMOF-74, CoMOF-74, and FeMOF-74 are available only for the lowest temperature of 318 K, the isotherm fits used for the simulations at 298 K are from the parameters presented by He et al.[18]

MgMOF-74 (= Mg_2 (dobdc) = Mg\(dobdc) with dobdc = (dobdc4– = 1,4-dioxido-2,5-benzenedicarboxylate)). This MOF consists of one-dimensional hexagonal-shaped channels with free internal diameter of ca. 11 Å

CoMOF-74 = (Co_2 (dobdc) = Co\(dobdc)) with dobdc = (dobdc4– = 1,4-dioxido-2,5-benzenedicarboxylate)). This MOF consists of one-dimensional hexagonal-shaped channels with free internal diameter of ca. 11 Å

FeMOF-74 (= Fe_2(dobdc) = Fe\(dobdc) with dobdc = (dobdc4– = 1,4-dioxido-2,5-benzenedicarboxylate)). This MOF consists of one-dimensional hexagonal-shaped channels with free internal diameter of ca. 11 Å

CuBTC (=$Cu_3(BTC)_2$ with BTC = 1,3,5-benzenetricarboxylate, also known as HKUST-1) structure consists of two types of "cages" and two types of "windows" separating these cages. Large cages are inter-connected by 9 Å windows of square cross-section. The large cages are also connected to tetrahedral-shaped pockets of ca. 6 Å size through triangular-shaped windows of ca. 4.6 Å size.

PAF-1-SO3Ag introduces π-complexation into highly porous PAF-122 with Ag(I) ions.[47]

MIL-101–Cr–SO3Ag was afforded via Ag(I) ion exchange of the sulphonic acid functionalized MIL-101–Cr.[48]

NOTT-300 = $[Al_2(OH)_2(C_{16}O_8H_6)]$.[33, 43] It has 6.5 Å × 6.5 Å channels. The isotherm data are available at 293 K.[43]

15. O_2/N_2 separations

MOF	Surface area $m^2\ g^{-1}$	Pore volume $cm^3\ g^{-1}$	Framework density $kg\ m^{-3}$	Data sources for unary isotherm fits	Comment
LTA-4A = RS-10	900	0.25	1529	[49, 50]	Diffusional effects are significant. Inter-cage hopping occurs one-molecule-at-a-time
LTA-5A	900	0.25	1508	[51-53]	Diffusional effects are significant. Inter-cage hopping occurs one-molecule-at-a-time
FeMOF-74	1536	0.626	1126	[54]	Diffusional effects are not of significant importance

LTA consists of 743.05 $Å^3$ size cages separated by 4 Å windows.

The adsorption and diffusion data for LTA-4A are for commercially available RS-10 that is a modified version of LTA-4A that affords higher diffusion selectivity in favor of O2; the data are taken from Farooq et al. [49, 50]

FeMOF-74 (= Fe_2(dobdc) = Fe\(dobdc) with dobdc = (dobdc4– = 1,4-dioxido-2,5-benzenedicarboxylate)). This MOF consists of one-dimensional hexagonal-shaped channels with free internal diameter of ca. 11 Å

Further simulation details are provided in our earlier work.[5]

16. N_2/CH_4 separations

MOF	Surface area $m^2\ g^{-1}$	Pore volume $cm^3\ g^{-1}$	Framework density $kg\ m^{-3}$	Data sources for unary isotherm fits	Comment
LTA-4A	900	0.25	1529	[55]	Diffusional effects are significant. Inter-cage hopping occurs one-molecule-at-a-time

LTA consists of 743.05 $Å^3$ size cages separated by 4 Å windows.

The simulation details are provided in our earlier work.[5] In these simulations the published data on unary isotherms and diffusivities[55] are used.

17. Separation of hexane isomers

MOF	Surface area $m^2\ g^{-1}$	Pore volume $cm^3\ g^{-1}$	Framework density $kg\ m^{-3}$	Data sources for unary isotherm fits	Comment
MFI	658	0.165	1796	CBMC simulations of isotherms at 433 K.[5]	Diffusional effects are significant for guest diffusion in the 5.5 Å channels.
ZIF-77	541	0.189	1553		Diffusional effects are significant for guest diffusion in the 4.5 Å channels.
$Fe_2(BDP)_3$		0.25	1145	Experimental data of Herm at 403 K, 433 K, and 473 K. These data are fitted with *T*-dependent parameters.[5]	Diffusional effects are significant for guest diffusion in the 4.9 Å triangular channels.

The simulation details are provided in our earlier work.[5]

MFI zeolite consists of 10-ring intersecting channels of 5.1 Å – 5.5 Å and 5.3 Å – 5.6 Å size.

The modelling of diffusion within the intersecting channels of MFI zeolite need to take proper account of synergy between adsorption and diffusion. For this purpose, the thermodynamic correction factors need to be accounted for, as described in detail in our earlier work.

$Fe_2(BDP)_3$ has one-dimensional triangular-shaped channels with free internal diameter of ca. 4.9 Å.

The main manuscript presents calculations of the RON of the gas exiting the fixed bed adsorber. These calculations are bassed on the transient breakthrough characteristics (cf Figure 14), with inclusion of diffusional limitations, for 5-component nC6/2MP/3MP/22DMB/23DMB mixture in a fixed bed adsorber packed with (a) Fe2(BDP)3, (b) ZIF-77, and (c) MFI zeolite a total pressure of 100 kPa and 433 K. The partial pressures of the components in the bulk gas phase operating at the inlet are $p_1 = p_2 = p_3 = p_4 = p_5 = 20$ kPa.

18. Separations of xylene isomers

MOF	Surface area $m^2\ g^{-1}$	Pore volume $cm^3\ g^{-1}$	Framework density $kg\ m^{-3}$	Data sources for unary isotherm fits	Comment
MAF-X8	1465	0.4947	954.29	CBMC simulated isotherms at 433 K.[56]	
BaX zeolite			1480	Experimental data at 393 K and 453 K. [57, 58]	
DynaMOF-100		0.626	1105	Experimental data on pure component isotherms at 298 K.[59]	
Mg-CUK-1	602	0.626	1142	Experimental data on pure component isotherms at 323 K.[60]	

MAF-X8 is a Zn(II) pyrazolate-carboxylate framework whose synthesis has been reported by He et al. [61] Within the one-dimensional 10 Å channels of MAF-X8, we have commensurate stacking of p-xylene.[56]

BaX is a cation-exchanged Faujasite zeolite. The FAU topology consists of 785.7 Å3 size cages separated by 7.4 Å size windows. Cage size is calculated on the basis of the equivalent sphere volume.

DynaMOF-100 consists of a Zn(II)-based dynamic coordination framework, [Zn4O(L)3] where the ligand L = 4, 4'- ((4-(tert-butyl) - 1,2- phenylene)bis(oxy))dibenzoate)

Mg-CUK-1 is the Mg(II) version of the porous coordination polymer CUK-1, synthesized by Saccoccia et al. [60] It has 1D pores of 8 Å size. It is to be noted that the isotherm data for Mg-CUK-1 is not available for ethylbenzene. In this case we adopt the following definition of selectivity for o-xylene(1)/m-xylene(2)/p-xylene(3) mixtures

$$S_{ads} = \frac{(q_3)/(q_1+q_2)}{(p_3)/(p_1+p_2)} = 2\frac{(q_3)}{(q_1+q_2)}$$

19. Styrene/ethylbenzene separations

MOF	Surface area $m^2\ g^{-1}$	Pore volume $cm^3\ g^{-1}$	Framework density $kg\ m^{-3}$	Data sources for unary isotherm fits	Comment
MIL-47(V)			1004	Experimental data at 298 K.[62] The original experiment data has been refitted; these parameters are used. [59]	The original experiment data has been refitted; [59] these parameters are used.
MIL-53(Al)			1041		
DynaMOF-100		0.626	1105	Experimental data on pure component isotherms at 298 K.[59]	

DynaMOF-100 consists of a Zn(II)-based dynamic coordination framework, [Zn4O(L)3] where the ligand L = 4, 4'- ((4-(tert-butyl) - 1,2- phenylene)bis(oxy))dibenzoate)

MIL-47 has one-dimensional diamond-shaped channels with free internal diameter of ca 8.5 Å

MIL-53 has one-dimensional diamond-shaped channels with free internal diameter of ca 8.5 Å

20. Benzene/cyclohexane separations

MOF	Surface area $m^2\ g^{-1}$	Pore volume $cm^3\ g^{-1}$	Framework density $kg\ m^{-3}$	Data sources for unary isotherm fits	Comment
AgY zeolite			1400	Data is available at 393 K;[63]	The experiment data has been refitted; these parameters are used.
PAF-2			740	Ren et al.[64]	
MnTriazolate			1422	Lin et al.[65]	

Cyclohexane, and important industrial chemical, is produced by catalytic hydrogenation of benzene. The unreacted benzene is present in the effluent from the reactor must be removed from the desired product. The separation of benzene and cyclohexane is difficult because the differences in the boiling points is only 0.6 K (cf. Figure 15). Currently technologies use extractive distillation with entrainers such as sulpholane, dimethylsulfoxide, N-methylpyrrolidone, and N-formylmorpholine; such processes are energy intensive. Adsorptive separations offer the energy-efficient alternatives to extractive distillation, especially for mixtures containing small percentage of benzene, as is commonly encountered.

Takahashi and Yang[63] have presented pure component isotherm data for benzene and cyclohexane to show that cation-exchange Faujasites Na-Y, Pd-Y, and Ag-Y zeolites have high selectivity for adsorption of benzene, due to π-complexation; cyclohexane does not form π-complexes.

An alternative to cation-exchange Faujasites, as suggested by Ren et al.[64] is to use a porous aromatic framework, PAF-2. The pure component isotherm data for PAF-2 shown in Figure 2b of Ren et al.[64] indicate that the saturation capacity of benzene is much higher than that of cyclohexane; this is perhaps due to molecular packing effects. Figure 15 shows the molecular structures of benzene and cyclohexane; it appears that stacking of flat benzene molecules is easier than stacking cyclohexanes in either the boat or chair configurations. In addition to molecular packing effects, the higher π–π interaction between the benzene molecule and the aromatic framework of PAF-2 also contributes to good separations.

Lin et al.[65] present the pure component isotherm data for benzene and cyclohexane for Mn triazolate MOF that also indicates a sign indicate that the saturation capacity of benzene is much higher than that of cyclohexane.

Figure 16 compares the transient breakthrough characteristics, for benzene/cyclohexane mixtures in fixed bed adsorbers packed with (a) AgY zeolite operating at 393 K, (b) PAF-2 operating at 298 K, and (c) MnTriazolate operating at 298 K. Since the data are not at the same temperatures it is difficult to compare these in a proper manner. Of the two MOFs investigated, MnTriazolate appears to have superior separation capabilities.

21. Notation

A	cross-sectional area of breakthrough tube, m^2
c_i	molar concentration of species i in gas mixture, mol m^{-3}
c_{i0}	molar concentration of species i in gas mixture at inlet to adsorber, mol m^{-3}
d	internal diameter of breakthrough tube, m
$Đ_i$	Maxwell-Stefan diffusivity, m^2 s^{-1}
L	length of packed bed adsorber, m
m_{ads}	mass of adsorbent packed into the breakthrough apparatus, kg
n	number of species in the mixture, dimensionless
N_i	molar flux of species i, mol m^{-2} s^{-1}
p_i	partial pressure of species i in mixture, Pa
p_t	total system pressure, Pa
q_i	component molar loading of species i, mol kg^{-1}
$q_{i,sat}$	molar loading of species i at saturation, mol kg^{-1}
q_t	total molar loading in mixture, mol kg^{-1}
$q_{sat,A}$	saturation loading of site A, mol kg^{-1}
$q_{sat,B}$	saturation loading of site B, mol kg^{-1}
$\bar{q}_i(t)$	*spatially averaged* component molar loading of species i, mol kg^{-1}
Q_{He}	volumetric flow rate of inert gas He, m^3 s^{-1}
Q_{st}	isosteric heat of adsorption, J mol^{-1}
Q_t	total volumetric flow rate, m^3 s^{-1}
r	radial direction coordinate, m
r_c	radius of crystallite, m
R	gas constant, 8.314 J mol^{-1} K^{-1}
t	time, s
T	absolute temperature, K

u	superficial gas velocity in packed bed, m s^{-1}
V_{ads}	volume of adsorbent packed into the breakthrough apparatus, m^3
y_i	mole fraction of species *i* in gas mixture, mol m^{-3}
z	distance along the adsorber, and along membrane layer, m

Greek letters

ε	voidage of packed bed, dimensionless
ρ	framework density, kg m^{-3}
τ	time, dimensionless
v	interstitial gas velocity in packed bed, m s^{-1}

22. References

(1) Bloch, E. D.; Queen, W. L.; Krishna, R.; Zadrozny, J. M.; Brown, C. M.; Long, J. R. Hydrocarbon Separations in a Metal-Organic Framework with Open Iron(II) Coordination Sites, *Science* **2012**, *335*, 1606-1610.

(2) Herm, Z. R.; Wiers, B. M.; Van Baten, J. M.; Hudson, M. R.; Zajdel, P.; Brown, C. M.; Maschiocchi, N.; Krishna, R.; Long, J. R. Separation of Hexane Isomers in a Metal-Organic Framework with Triangular Channels *Science* **2013**, *340*, 960-964.

(3) Gücüyener, C.; van den Bergh, J.; Gascon, J.; Kapteijn, F. Ethane/Ethene Separation Turned on Its Head: Selective Ethane Adsorption on the Metal-Organic Framework ZIF-7 through a Gate-Opening Mechanism, *J. Am. Chem. Soc.* **2010**, *132*, 17704-17706.

(4) Yang, J.; Krishna, R.; Li, J.; Li, J. Experiments and Simulations on Separating a CO_2/CH_4 Mixture using K-KFI at Low and High Pressures, *Microporous Mesoporous Mater.* **2014**, *184*, 21-27.

(5) Krishna, R. The Maxwell-Stefan Description of Mixture Diffusion in Nanoporous Crystalline Materials, *Microporous Mesoporous Mater.* **2014**, *185*, 30-50.

(6) Krishna, R.; Long, J. R. Screening metal-organic frameworks by analysis of transient breakthrough of gas mixtures in a fixed bed adsorber, *J. Phys. Chem. C* **2011**, *115*, 12941-12950.

(7) Krishna, R.; Baur, R. Modelling issues in zeolite based separation processes, *Sep. Purif. Technol.* **2003**, *33*, 213-254.

(8) Krishna, R. Separating Mixtures by Exploiting Molecular Packing Effects in Microporous Materials, *Phys. Chem. Chem. Phys.* **2015**, *17*, 39-59.

(9) Gu, Z.-Y.; Yang, C.-X.; Chang, N.; Yan, X.-P. Metal-Organic Frameworks for Analytical Chemistry: From Sample Collection to Chromatographic Separation, *Acc. Chem. Res.* **2012**, *45*, 734-745.

(10) Chang, N.; Gu, Z.-Y.; Yan, X.-P. Zeolitic Imidazolate Framework-8 Nanocrystal Coated Capillary for Molecular Sieving of Branched Alkanes from Linear Alkanes along with High-Resolution Chromatographic Separation of Linear Alkanes, *J. Amer. Chem. Soc.* **2010**, *132*, 13645-13647.

(11) Gu, Z. Y.; Yan, X. P. Metal–Organic Framework MIL-101 for High-Resolution Gas-Chromatographic Separation of Xylene Isomers and Ethylbenzene, *Angew. Chem. Int. Ed.* **2010**, *49*, 1477-1480.

(12) Gu, Z. Y.; Jiang, D. Q.; Wang, H. F.; Cui, X. Y.; Yan, X. P. Adsorption and Separation of Xylene Isomers and Ethylbenzene on Two Zn-Terephthalate Metal-Organic Frameworks, *J. Phys. Chem. C* **2010**, *114*, 311-316.

(13) Myers, A. L.; Prausnitz, J. M. Thermodynamics of Mixed Gas Adsorption, *A.I.Ch.E.J.* **1965**, *11*, 121-130.

(14) Chen, D.-L.; Shang, H.; Zhu, W.; Krishna, R. Transient Breakthroughs of CO_2/CH_4 and C_3H_6/C_3H_8 Mixtures in Fixed Beds packed with Ni-MOF-74, *Chem. Eng. Sci.* **2014**, *117*, 407-415.

(15) Yu, H.; Wang, X.; Xu, C.; Chen, D.-L.; Zhu, W.; Krishna, R. Utilizing transient breakthroughs for evaluating the potential of Kureha carbon for CO_2 capture, *Chem. Eng. J.* **2015**, *269*, 135-147.

(16) Li, P.; He, Y.; Zhao, Y.; Weng, L.; Wang, H.; Krishna, R.; Wu, H.; Zhou, W.; O'Keeffe, M.; Han, Y.; Chen, B. A Rod-Packing Microporous Hydrogen-Bonded Organic Framework for Highly Selective Separation of C_2H_2/CO_2 at Room Temperature, *Angew. Chem. Int. Ed.* **2015**, *54*, 574-577.

(17) Duan, X.; Zhang, Q.; Cai, J.; Yang, Y.; Cui, Y.; He, Y.; Wu, C.; Krishna, R.; Chen, B.; Qian, G. A New Metal–Organic Framework with Potential for Adsorptive Separation of Methane from

Carbon Dioxide, Acetylene, Ethylene, and Ethane Established by Simulated Breakthrough Experiments, *J. Mater. Chem. A* **2014**, *2*, 2628-2633.

(18) He, Y.; Krishna, R.; Chen, B. Metal-Organic Frameworks with Potential for Energy-Efficient Adsorptive Separation of Light Hydrocarbons, *Energy Environ. Sci.* **2012**, *5*, 9107-9120.

(19) Kong, G. Q.; Han, Z. D.; He, Y.; Qu, S.; Zhou, W.; Yildirim, T.; Krishna, R.; Zou, C.; Wu, C. D.; Chen, B. Expanded Organic Building Units for the Construction of Highly Porous Metal-Organic Frameworks, *Chem. Eur. J.* **2013**, *19*, 14886-14894.

(20) Duan, J.; Jin, W.; Krishna, R. Natural Gas Purification Using a Porous Coordination Polymer with Water and Chemical Stability, *Inorg. Chem.* **2015**, *54*, 4279-4284.

(21) Xia, T.; Cai, J.; Wang, H.; Duan, X.; Cui, Y.; Yang, Y.; Qian, G. Microporous Metal-Organic Frameworks with Suitable Pore Spaces for Acetylene Storage and Purification, *Microporous Mesoporous Mater.* **2015**, *XXX*, XXX-XXX. http://dx.doi.org/doi:10.1016/j.micromeso.2015.05.036.

(22) Liu, J.; Strachan, D. M.; Thallapally, P. K. Enhanced noble gas adsorption in Ag@MOF-74Ni, *Chem. Commun.* **2014**, *50*, 466-468.

(23) Liu, J.; Thallapally, P. K.; Strachan, D. Metal−Organic Frameworks for Removal of Xe and Kr from Nuclear Fuel Reprocessing Plants, *Langmuir* **2012**, *28*, 11584-11589.

(24) Gurdal, Y.; Keskin, S. Atomically Detailed Modeling of Metal Organic Frameworks for Adsorption, Diffusion, and Separation of Noble Gas Mixtures, *Ind. Eng. Chem. Res.* **2012**, *51*, 7373-8382.

(25) Chen, X.; Plonka, A. M.; Banerjee, D.; Krishna, R.; Schaef, H. T.; Ghose, D.; Thallapally, P. K.; Parise, J. B. Direct Observation of Xe and Kr Adsorption in a Xe-selective Microporous Metal Organic Framework, *J. Am. Chem. Soc.* **2015**, *XX*, XXX-XXX. http://dx.doi.org/doi:10.1021/jacs.5b02556.

(26) Wang, H.; Yao, K.; Zhang, Z.; Jagiello, J.; Gong, Q.; Han, Y.; Li, J. The First Example of Commensurate Adsorption of Atomic Gas in a MOF and Effective Separation of Xenon from Other Noble Gases, *Chem. Sci.* **2014**, *5*, 620-624.

(27) Mason, J. A.; Sumida, K.; Herm, Z. R.; Krishna, R.; Long, J. R. Evaluating Metal-Organic Frameworks for Post-Combustion Carbon Dioxide Capture via Temperature Swing Adsorption, *Energy Environ. Sci.* **2011**, *4*, 3030-3040.

(28) Dietzel, P. D. C.; Besikiotis, V.; Blom, R. Application of metal–organic frameworks with coordinatively unsaturated metal sites in storage and separation of methane and carbon dioxide, *J. Mater. Chem.* **2009**, *19*, 7362-7370.

(29) Krishna, R.; van Baten, J. M. Investigating the Relative Influences of Molecular Dimensions and Binding Energies on Diffusivities of Guest Species Inside Nanoporous Crystalline Materials *J. Phys. Chem. C* **2012**, *116*, 23556-23568.

(30) Belmabkhout, Y.; Pirngruber, G.; Jolimaitre, E.; Methivier, A. A complete experimental approach for synthesis gas separation studies using static gravimetric and column breakthrough experiments, *Adsorption* **2007**, *13*, 341-349.

(31) Hudson, M. R.; Murray, L.; Mason, J. A.; Fickel, D. W.; Lobo, R. F.; Queen, W. L.; Brown, C. M. Unconventional and Highly Selective CO_2 Adsorption in Zeolite SSZ-13, *J. Am. Chem. Soc.* **2012**, *134*, 1970-1973.

(32) Xiang, S. C.; He, Y.; Zhang, Z.; Wu, H.; Zhou, W.; Krishna, R.; Chen, B. Microporous Metal-Organic Framework with Potential for Carbon Dioxide Capture at Ambient Conditions, *Nat. Commun.* **2012**, *3*, 954. http://dx.doi.org/doi:10.1038/ncomms1956.

(33) Yang, S.; Sun, J.; Ramirez-Cuesta, A. J.; Callear, S. K.; David, W. I. F.; Anderson, D. P.; Newby, R.; Blake, A. J.; Parker, J. E.; Tang, C. C.; Schröder, M. Selectivity and direct visualization of carbon dioxide and sulfur dioxide in a decorated porous host, *Nature Chemistry* **2012**, *4*, 887-894.

(34) Krishna, R. Adsorptive separation of $CO_2/CH_4/CO$ gas mixtures at high pressures, *Microporous Mesoporous Mater.* **2012**, *156*, 217-223.

(35) Wu, H.; Yao, K.; Zhu, Y.; Li, B.; Shi, Z.; Krishna, R.; Li, J. Cu-TDPAT, an *rht*-type Dual-Functional Metal–Organic Framework Offering Significant Potential for Use in H_2 and Natural Gas Purification Processes Operating at High Pressures, *J. Phys. Chem. C* **2012**, *116*, 16609-16618.

(36) Chavan, S.; Bonino, F.; Valenzano, L.; Civalleri, B.; Lamberti, C.; Acerbi, N.; Cavka, J. H.; Leistner, M.; Bordiga, S. Fundamental Aspects of H_2S Adsorption on CPO-27-Ni, *J. Phys. Chem. C* **2013**, *117*, 15615-15622.

(37) Vaesen, S.; Guillerm, V.; Yang, Q.; Wiersum, A. D.; Marszalek, B.; Gil, B.; Vimont, A.; Daturi, M.; Devic, T.; Llewellyn, P. L.; Serre, C.; Maurin, G.; De Weireld, G. A robust amino-functionalized titanium(IV) based MOF for improved separation of acid gases, *Chem. Commun.* **2013**, *49*, 10082-10084.

(38) Agueda, V. I.; Delgado, J. A.; Uguina, M. A.; Brea, P.; Spjelkavik, A. I.; Blom, R.; Grande, C. Adsorption and diffusion of H_2, N_2, CO, CH_4 and CO_2 in UTSA-16 metal-organic framework extrudates, *Chem. Eng. Sci.* **2015**, *124*, 159-169.

(39) Moellmer, J.; Moeller, A.; Dreisbach, F.; Glaeser, R.; Staudt, R. High pressure adsorption of hydrogen, nitrogen, carbon dioxide and methane on the metal–organic framework HKUST-1, *Microporous Mesoporous Mater.* **2011**, *138*, 140-148.

(40) Banu, A. M.; Friedrich, D.; Brandani, S.; Düren, T. A Multiscale Study of MOFs as Adsorbents in H_2 PSA Purification, *Ind. Eng. Chem. Res.* **2013**, *52*, 9946-9957.

(41) Silva, B.; Salomon, I.; Ribeiro, A. M.; Chang, J. S.; Loureiro, J. M.; Rodrigues, A. E. H_2 purification by Pressure Swing Adsorption using CuBTC, *Sep. Purif. Technol.* **2013**, *118*, 744-756.

(42) Majlan, E. H.; Daud, W. R. W.; Iyuke, S. E.; Mohamad, A. B.; Kadhum, A. H.; Mohammad, A. W.; Takriff, M. S.; Bahaman, N. Hydrogen purification using compact pressure swing adsorption system for fuel cell, *Int. J. Hydrogen Energy* **2009**, *34*, 2771-2777.

(43) Yang, S.; Ramirez-Cuesta, A. J.; Newby, R.; Garcia-Sakai, V.; Manuel, P.; Callear, S. K.; Campbell, S. I.; Tang, C. C.; Schröder, M. Supramolecular binding and separation of hydrocarbons within a functionalized porous metal–organic framework, *Nature Chemistry* **2014**, *7*, 121-129.

(44) Hu, T.-L.; Wang, H.; Li, B.; Krishna, R.; Wu, H.; Zhou, W.; Zhao, Y.; Han, Y.; Wang, X.; Zhu, W.; Yao, Z.; Xiang, S. C.; Chen, B. A microporous metal-organic framework with dual functionalities for highly efficient removal of acetylene from ethylene/acetylene mixtures at room temperature, *Nat. Commun.* **2015**, *6*, 7328. http://dx.doi.org/doi:10.1038/ncomms8328.

(45) Das, M. C.; Guo, Q.; He, Y.; Kim, J.; Zhao, C. G.; Hong, K.; Xiang, S.; Zhang, Z.; Thomas, K. M.; Krishna, R.; Chen, B. Interplay of Metalloligand and Organic Ligand to Tune Micropores within Isostructural Mixed-Metal Organic Frameworks (M'MOFs) for Their Highly Selective Separation of Chiral and Achiral Small Molecules, *J. Am. Chem. Soc.* **2012**, *134*, 8703-8710.

(46) Geier, S. J.; Mason, J. A.; Bloch, E. D.; Queen, W. L.; Hudson, M. R.; Brown, C. M.; Long, J. R. Selective adsorption of ethylene over ethane and propylene over propane in the metal–organic frameworks M_2(dobdc) (M = Mg, Mn, Fe, Co, Ni, Zn), *Chem. Sci.* **2013**, *4*, 2054-2061.

(47) Li, B.; Zhang, Y.; Krishna, R.; Yao, K.; Han, Y.; Wu, Z.; Ma, D.; Shi, Z.; Pham, T.; Space, B.; Liu, J.; Thallapally, P. K.; Liu, J.; Chrzanowski, M.; Ma, S. Introduction of Π-Complexation into Porous Aromatic Framework for Highly Selective Adsorption of Ethylene over Ethane, *J. Am. Chem. Soc.* **2014**, *136*, 8654-8660.

(48) Zhang, Y.; Li, B.; Krishna, R.; Wu, Z.; Ma, D.; Shi, Z.; Pham, T.; Forrest, K.; Space, B.; Ma, S. Highly Selective Adsorption of Ethylene over Ethane in a MOF Featuring the Combination of Open Metal Site and π-Complexation, *Chem. Commun.* **2015**, *51*, 2714-2717.

(49) Farooq, S.; Rathor, M. N.; Hidajat, K. A Predictive Model for a Kinetically Controlled Pressure Swing Adsorption Separation Process, *Chem. Eng. Sci.* **1993**, *48*, 4129-4141.

(50) Farooq, S. Sorption and Diffusion of Oxygen and Nitrogen in Molecular- Sieve RS-10, *Gas Sep. Purif.* **1995**, *9*, 205-212.

(51) Rama Rao, V.; Farooq, S.; Krantz, W. B. Design of a Two-Step Pulsed Pressure-Swing Adsorption-Based Oxygen Concentrator, *A.I.Ch.E.J.* **2010**, *56*, 354-370.

(52) Rama Rao, V. Adsorption based portable oxygen concentrator for personal medical applications, Ph.D. Dissertation, National University of Singapore, Singapore, 2011.

(53) Farooq, S.; Ruthven, D. M.; Boniface, H. A. Numerical-Simulation of a Pressure Swing Adsorption Oxygen Unit, *Chem. Eng. Sci.* **1989**, *44*, 2809-2816.

(54) Bloch, E. D.; Murray, L.; Queen, W. L.; Chavan, S. M.; Maximoff, S. N.; Bigi, J. P.; Krishna, R.; Peterson, V. K.; Grandjean, F.; Long, G. J.; Smit, B.; Bordiga, S.; Brown, C. M.; Long, J. R. Selective Binding of O_2 over N_2 in a Redox-Active Metal-Organic Framework with Open Iron(II) Coordination Sites, *J. Am. Chem. Soc.* **2011**, *133*, 14814-14822.

(55) Habgood, H. W. The Kinetics of Molecular Sieve Action. Sorption of Nitrogen-Methane Mixtures by Linde Molecular Sieve 4A, *Canad. J. Chem.* **1958**, *36*, 1384-1397.

(56) Torres-Knoop, A.; Krishna, R.; Dubbeldam, D. Separating Xylene Isomers by Commensurate Stacking of p-Xylene within Channels of MAF-X8, *Angew. Chem. Int. Ed.* **2014**, *53*, 7774-7778.

(57) Minceva, M.; Rodrigues, A. E. Understanding and Revamping of Industrial Scale SMB Units for p-Xylene Separation, *A.I.Ch.E.J.* **2007**, *53*, 138-149.

(58) Minceva, M.; Rodrigues, A. E. Adsorption of xylenes on Faujasite-type zeolite. Equilibrium and Kinetics in Batch Adsorber, *Chem. Eng. Res. Des.* **2004**, *82*, 667-681.

(59) Mukherjee, S.; Joarder, B.; Desai, A. V.; Manna, B.; Krishna, R.; Ghosh, S. K. Exploiting Framework Flexibility of a Metal-Organic Framework for Selective Adsorption of Styrene over Ethylbenzene, *Inorg. Chem.* **2015**, *54*, 4403-4408.

(60) Saccoccia, B.; Bohnsack, A. M.; Waggoner, N. W.; Cho, K. H.; Lee, J. S.; Hong, D.-Y.; Lynch, V. M.; Chang, J.-S.; Humphrey, S. M. Separation of p-Divinylbenzene by Selective Room-Temperature Adsorption Inside Mg-CUK-1 Prepared by Aqueous Microwave Synthesis, *Angew. Chem. Int. Ed.* **2015**, *54*, 5394-5398.

(61) He, C.-T.; Tian, J. Y.; Liu, S. Y.; Ouyang, G.; Zhang, J.-P.; Chen, X. M. A porous coordination framework for highly sensitive and selective solid-phase microextraction of non-polar volatile organic compounds, *Chem. Sci.* **2013**, *4*, 351-356.

(62) Maes, M.; Vermoortele, F.; Alaerts, L.; Couck, S.; Kirschhock, C. E. A.; Denayer, J. F. M.; De Vos, D. E. Separation of Styrene and Ethylbenzene on Metal-Organic Frameworks: Analogous Structures with Different Adsorption Mechanisms, *J. Am. Chem. Soc.* **2010**, *132*, 15277-15285.

(63) Takahashi, A.; Yang, R. T. New Adsorbents for Purification: Selective Removal of Aromatics, *A.I.Ch.E.J.* **2002**, *48*, 1457-1468.

(64) Ren, H.; Ben, T.; Wang, E.; Jing, X.; Xue, M.; Liu, B.; Cui, Y.; Qui, S.; Zhu, G. Targeted synthesis of a 3D porous aromatic framework for selective sorption of benzene, *Chem. Commun.* **2010**, *46*, 291-293.

(65) Lin, J.-B.; Zhang, J.-P.; Zhang, W.-X.; Wei Xue, W.; Xue, D.-X.; Chen, X.-M. Porous Manganese(II) 3-(2-Pyridyl)-5-(4-Pyridyl)-1,2,4-Triazolate Frameworks: Rational Self-Assembly, Supramolecular Isomerism, Solid-State Transformation, and Sorption Properties, *Inorg. Chem.* **2009**, *46*, 6852-6660.

23. Caption for Figures

Figure 1. Schematic of a packed bed adsorber.

Figure 2. Schematic of the breakthrough tube. The tube diameter is 4.65 mm, and tube length L = 100 mm. The mass of adsorbent used in the bed is: NiMOF-74 = 576.1 mg, and Kureha carbon = 760 mg. The gas phase used in the experiments consisted of CO_2/CH_4/He mixtures. The gas phase compositions at the inlet were maintained at 25/25/50.The flow rate of He was maintained constant at 4 mL min^{-1} at STP conditions.

Figure 3. Experimental breakthroughs of Chen et al.[14] and Yu et al.[15] for CO_2(1)/CH_4(2)/He(3) mixtures in packed bed with NiMOF-74, and Kureha carbon at 298 K. The partial pressures at the inlet are $p_1 = p_2$ = 50 kPa; p_3 = 100 kPa. In (a) the y-axis represents the % CO_2 in the exit gas phase, excluding the presence of inert gas He. In (b) the y-axis represents the % CH_4 in the exit gas phase, excluding the presence of inert gas He. As indicated for NiMOF-74, it is possible to produce CH_4 with 99% purity during the time interval between t_1, and t_2. (c) The CO_2 captured is plotted against the dimensionless breakthrough time.

Figure 4. (a, b) Calculations using the Ideal Adsorbed Solution Theory (IAST) of (a) adsorption selectivity, S_{ads}, and (b) uptake capacity of C_2H_2, for separation of 50/50 C_2H_2/CO_2 mixture at 296 K

using HOF-3, CuBTC, ZJU-60a, PCP-33, and Cu_2TPTC-Me. (c) Comparison of % C_2H_2 in the exit gas for beds packed with HOF-3, CuBTC, ZJU-60a, and PCP-33 plottted as a function of the dimensionless breakthrough time.

Figure 5. Comparison of % CO_2 in the exit gas for fixed bed adsorber beds packed with different adsorbents, fed with 50/50 CO_2/CH_4 mixture, operating at 298 K and (a) p_t = 100 kPa, (b) p_t = 600 kPa, (c) p_t = 2 MPa.

Figure 6. Plots of the amount of CO_2 captured during the time interval 0 - τ_{break} as function of the dimensionless breakthrough time, τ_{break}, for fixed bed adsorber beds packed with different adsorbents, fed with 50/50 CO_2/CH_4 mixture, operating at 298 K and (a) p_t = 100 kPa, (b) p_t = 600 kPa, (c) p_t = 2 MPa. (c) 100 kPa, and (b) 2 MPa.

Figure 7. Adsorption/desorption breakthrough characteristics of 3-component 35.5/47/17.5 $H_2/CO_2/CH_4$ mixture in adsorber packed with CuBTC at 303 K operating at a total pressure of 0.2 MPa. The desorption phase is initiated at time t = 6550 s, the 3-component mixture is switched to pure H_2. The experimental data of Silva et al.[41] (symbols) are compared with breakthrough simulations (continuous solid lines) assuming thermodynamic equilibrium, i.e. invoking Equation (10). The experimental conditions correspond to Run 5 of Silva et al[41]: L = 0.31 m; voidage of bed, ε = 0.52; interstitial gas velocity, v = 0.0305 m/s. The isotherm data for CuBTC are from the Silva paper.

Figure 8. (a) Ppm (CO_2 + CO) in outlet gas as a function of the dimensionless time for separation of 3-component 73/16/11 $H_2/CO_2/CO$ mixtures using five different adsorbent materials. (b) Plot of the amount of H_2 produced (< 10 ppm impurities) per L of material during the time interval 0 - τ_{break} as function of the dimensionless breakthrough time, τ_{break} for separation of 3-component 73/16/11 $H_2/CO_2/CO$ mixtures.

Figure 9.(a) Ppm CO_2 in outlet gas as a function of the dimensionless time for separation of binary 50/50 CO_2/CO mixtures using five different adsorbent materials. (b) Plots of the amount of CO_2 captured (< 500 ppm impurities) per L of material during the time interval 0 - τ_{break} as function of the dimensionless breakthrough time, τ_{break}.

Figure 10. (a) IAST calculations of the adsorption selectivity, S_{ads}, of 50/50 C_2H_2/C_2H_4 mixtures using four different MOFs. (b) C_2H_2 uptake capacity of 50/50 C_2H_2/C_2H_4 mixtures. (c) Comparison of % C_2H_2 in the exit gas from adsorber beds. (d) Plot of the amount of C_2H_2 captured during the time interval 0 - τ_{break} as function of the dimensionless breakthrough time, τ_{break}.

Figure 11. (a, b) IAST calculations of (a) adsorption selectivity, S_{ads}, and (b) C_3H_6 uptake capacity in 50/50 C_2H_4/C_2H_6 mixtures at 318 K using six different M-MOF-74 with M = Fe, Co, Ni, Zn, and Mn. (c) Comparison of C_2H_4 in the exit gas from adsorber beds. (d) Plot of the amount of C_2H_4 captured during the time interval 0 - τ_{break} as function of the dimensionless breakthrough time, τ_{break}.

Figure 12. (a, b) IAST calculations of (a) adsorption selectivity, S_{ads}, and (b) C_3H_6 uptake capacity in 50/50 C_3H_6/C_3H_8 mixtures at 318 K using six different M-MOF-74 with M = Fe, Co, Ni, Zn, and Mn. (c) Comparison of % C_3H_6 in the exit gas from adsorber beds. (d) Plot of the amount of C_3H_6 captured during the time interval 0 - τ_{break} as function of the dimensionless breakthrough time, τ_{break}.

Figure 13. Isosteric heat of adsorption of (a, b) C_2H_4, and (c) C_3H_6 in a variety of MOFs.

Figure 14. Transient breakthrough characteristics, with inclusion of diffusional limitations, for 5-component nC6/2MP/3MP/22DMB/23DMB mixture in a fixed bed adsorber packed with (a) $Fe_2(BDP)_3$, (b) ZIF-77, and (c) MFI zeolite a total pressure of 100 kPa and 433 K. The partial pressures of the components in the bulk gas phase operating at the inlet are $p_1 = p_2 = p_3 = p_4 = p_5 = 20$ kPa.

Figure 15. Molecular structures of benzene and cyclohexane. Also indicated are the boiling points and freezing points.

Figure 16. Transient breakthrough characteristics, for benzene/cyclohexane mixtures in fixed bed adsorbers packed with (a) AgY zeolite operating at 393 K, (b) PAF-2 operating at 298 K, and (c) MnTriazolate operating at 298 K. The total pressure is 100 kPa.

ESI Figure 1

Fixed bed adsorber

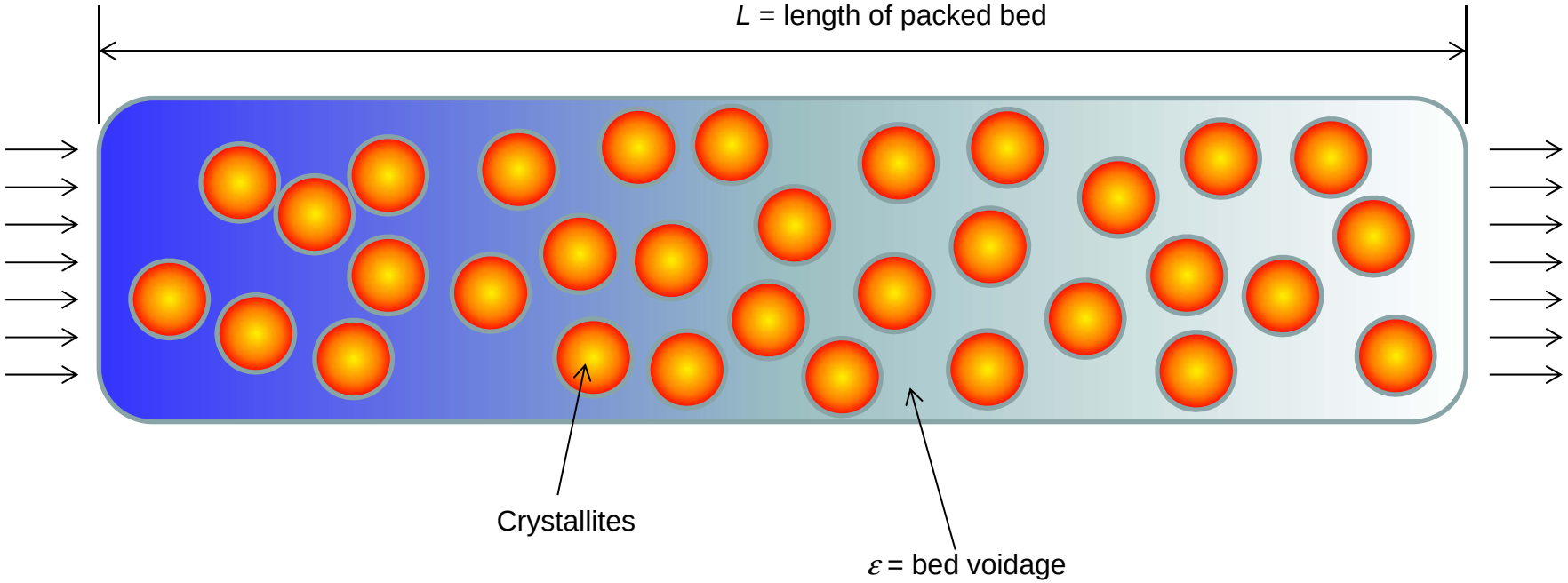

u =
superficial
gas
velocity

v = *u*/*ε* = interstitial gas velocity

L/*v* =
Characteristic time of contact between gas and liquid

ESI Figure 2

Breakthrough apparatus

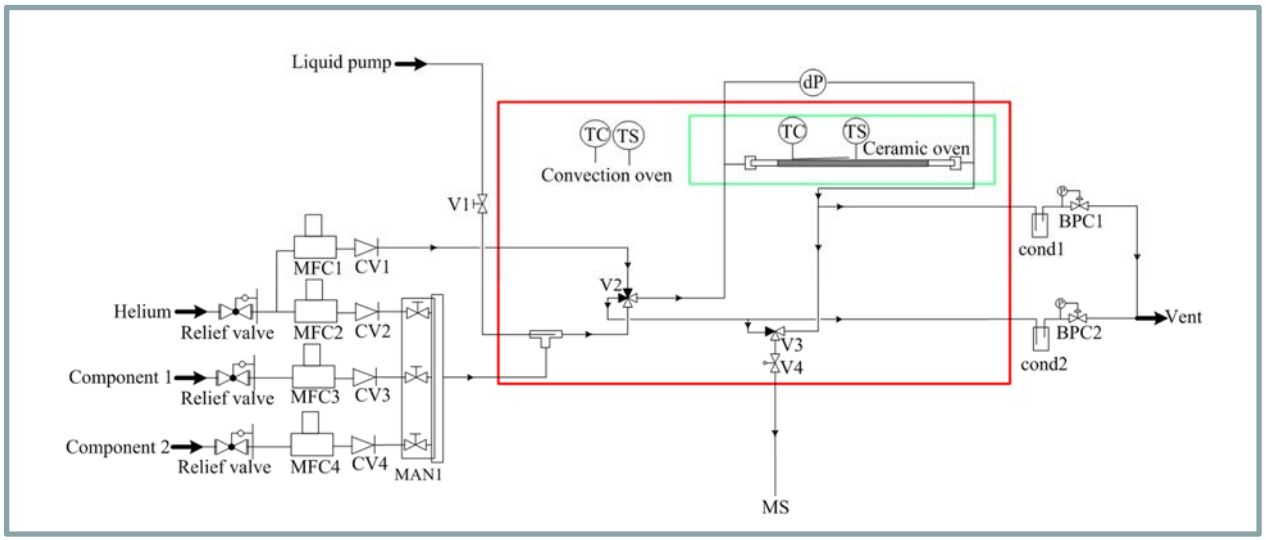

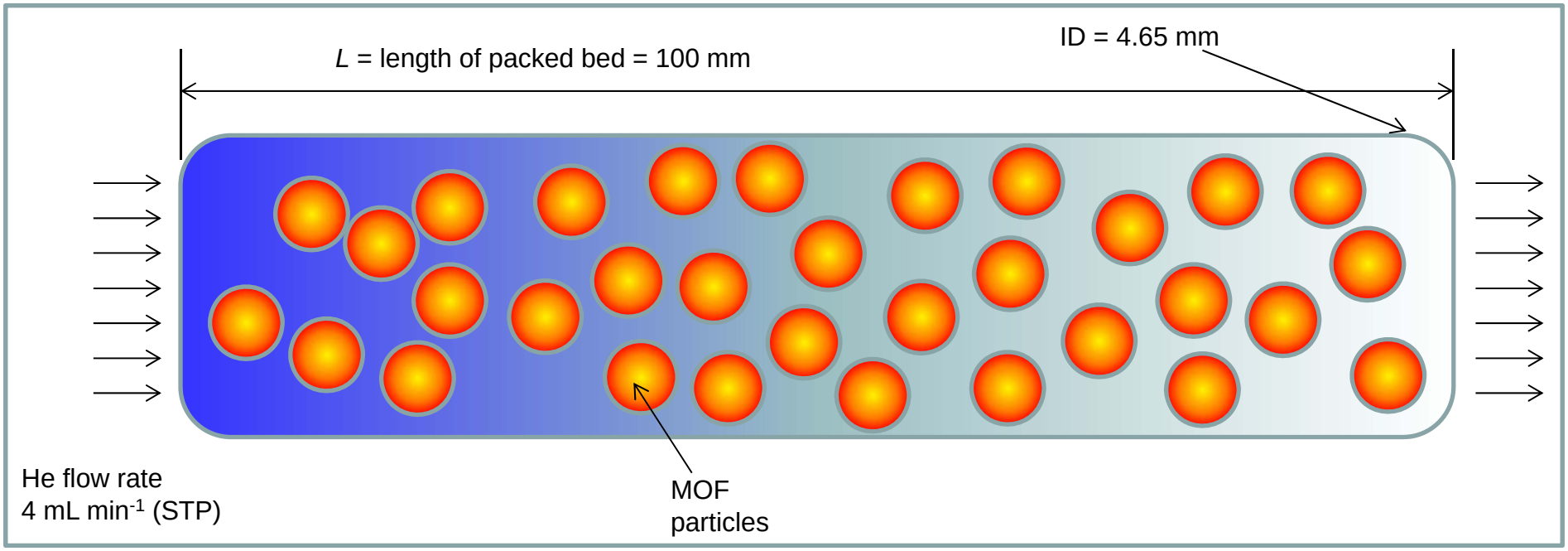

Breakthrough experiments

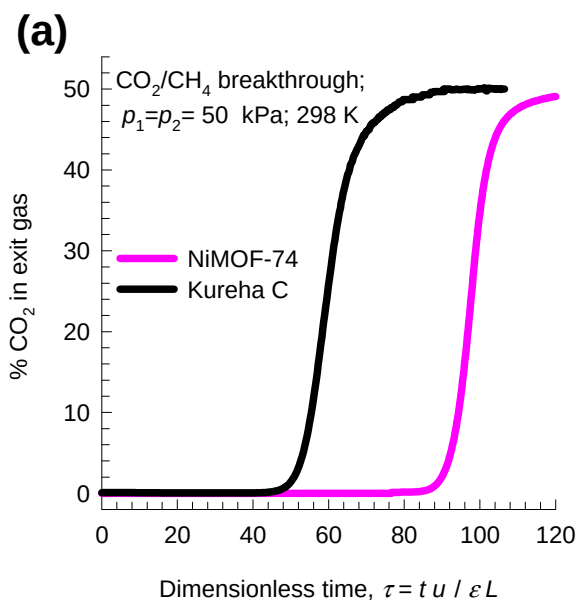

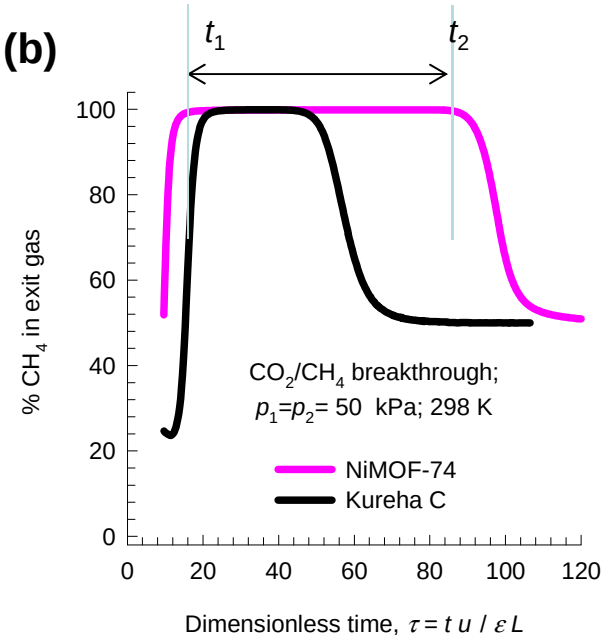

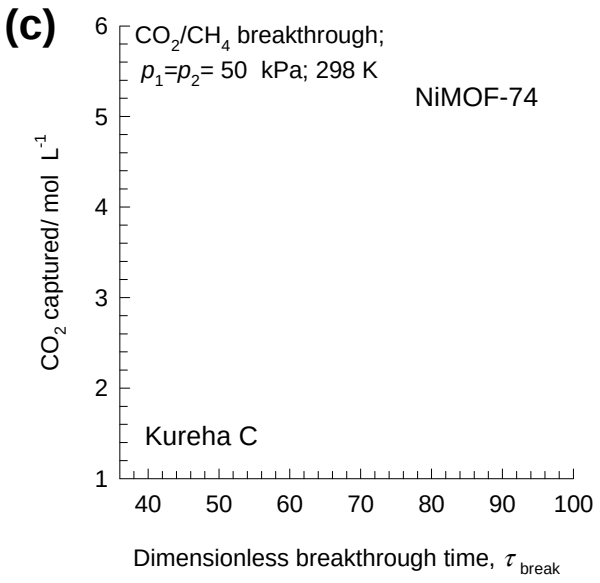

ESI Figure 4

C_2H_2/CO_2 separations: comparisons including Cu_2TPTC-Me

(a)

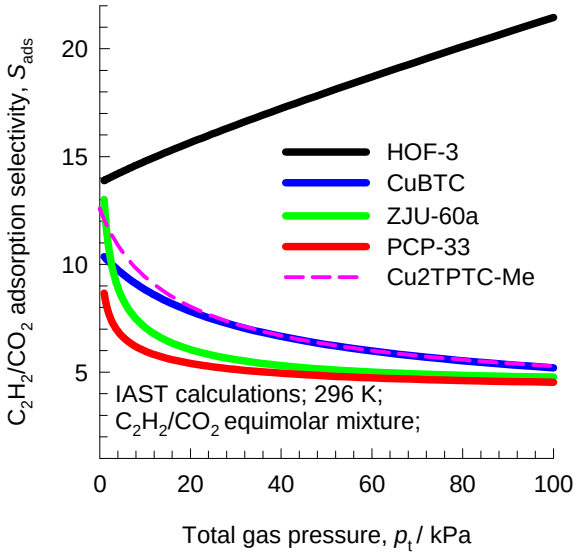

(b)

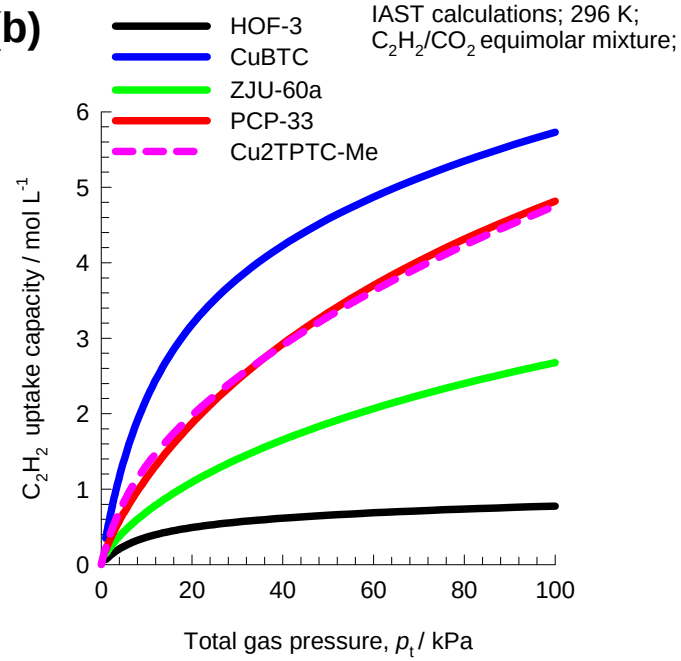

(c)

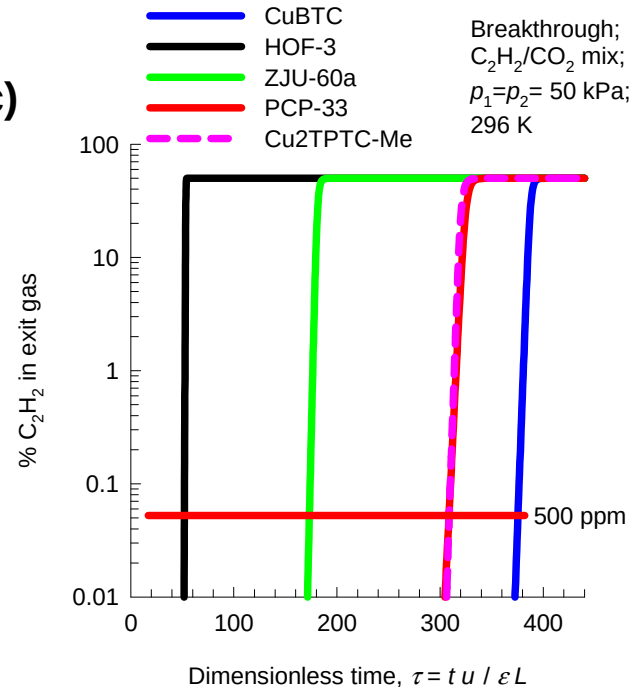

ESI Figure 5

CO_2/CH_4 separations at three different pressures

(a)

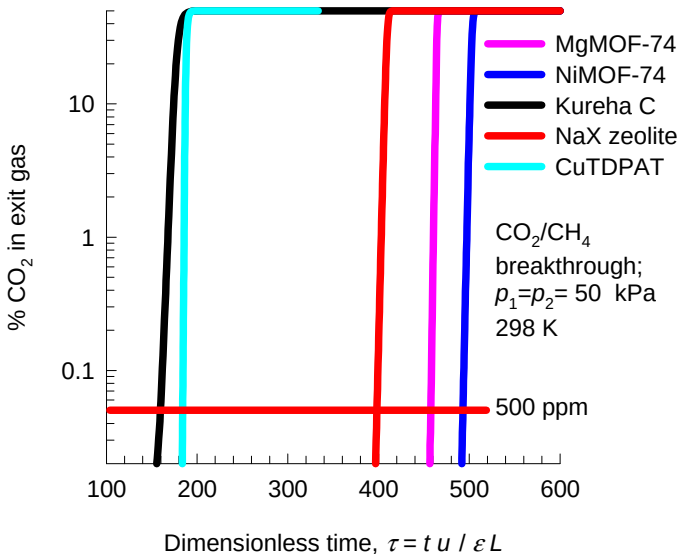

(b)

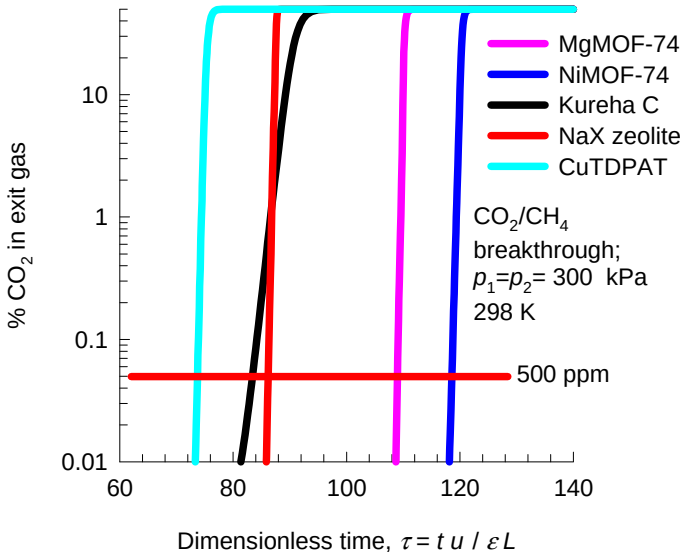

(c)

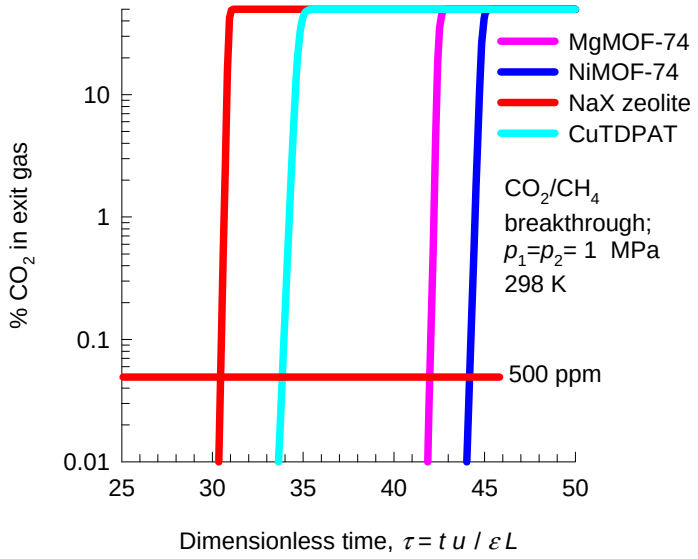

ESI Figure 6

CO_2/CH_4 separations at three different pressures

(a)

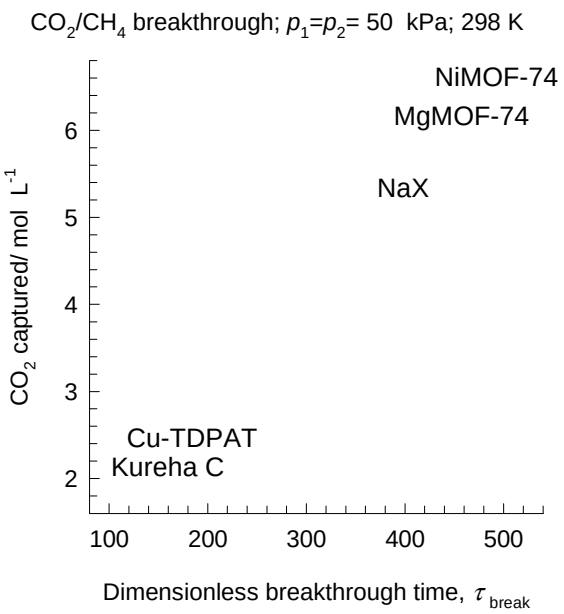

(b)

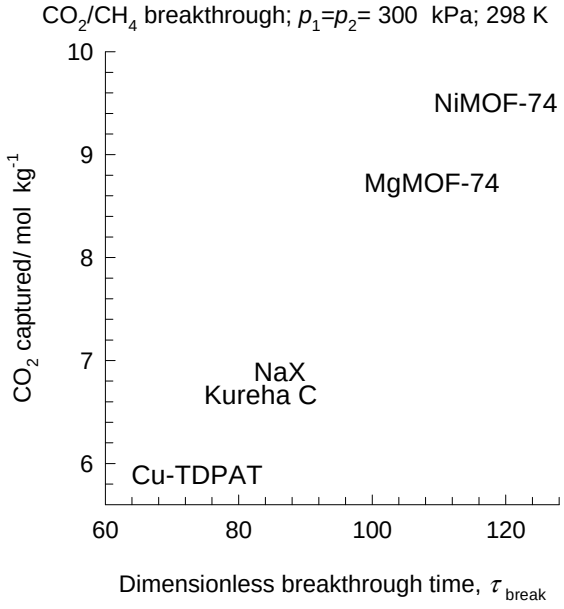

(c)

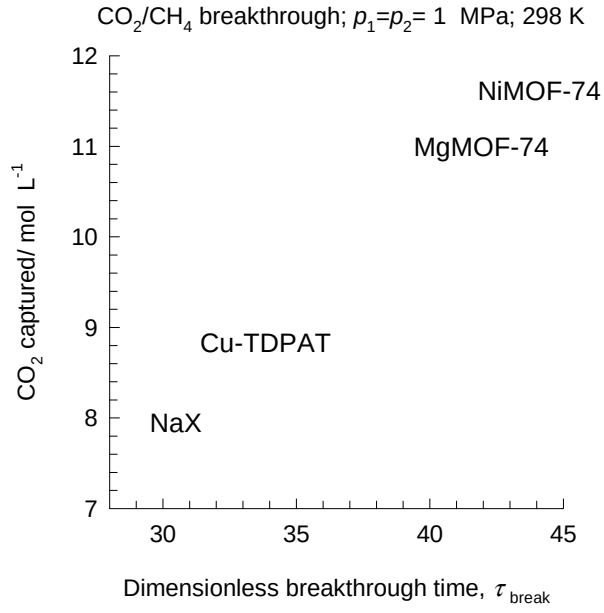

Breakthrough H_2 purification CuBTC

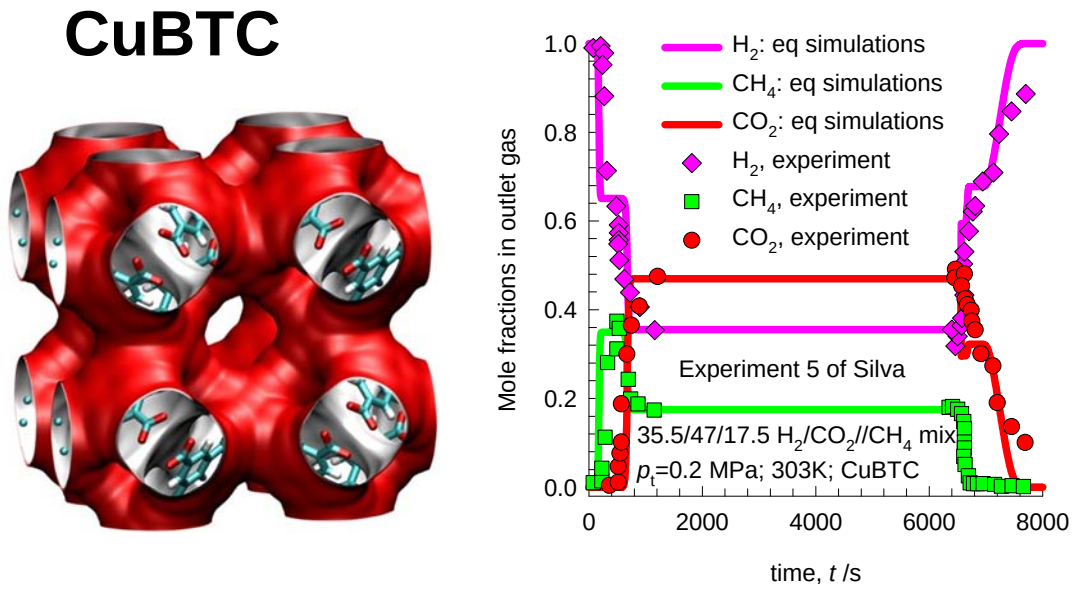

Fuel-cell grade H_2 production

ESI Figure 8

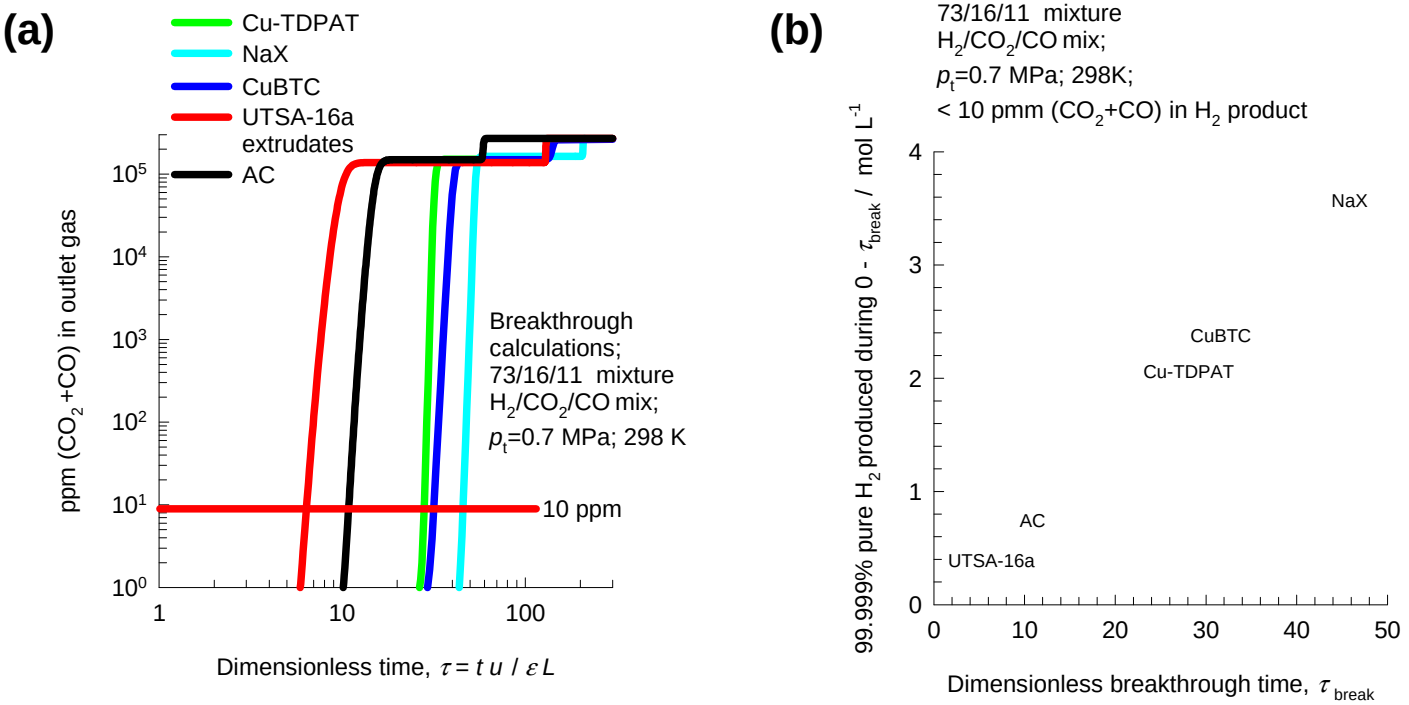

CO_2/CO mixture separations

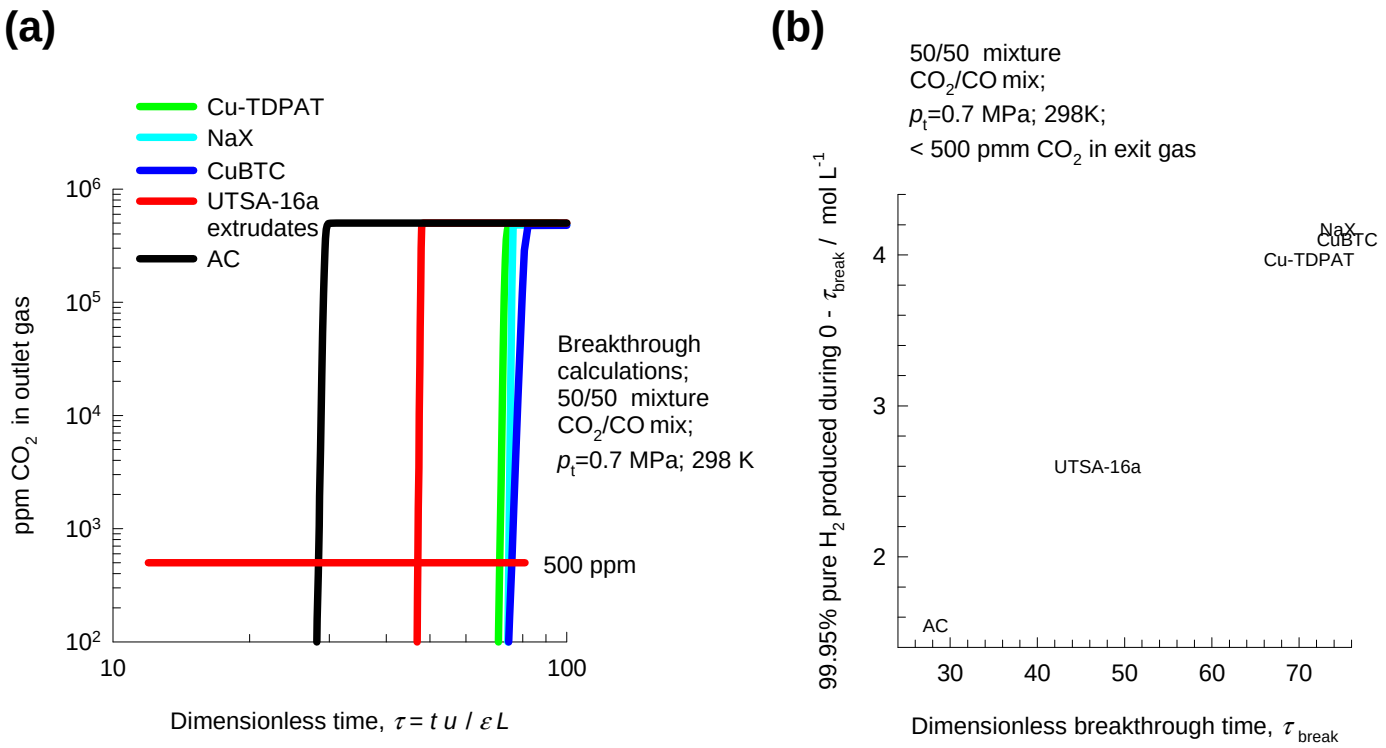

ESI Figure 10

C_2H_2/C_2H_4 separations for 50/50 mixtures

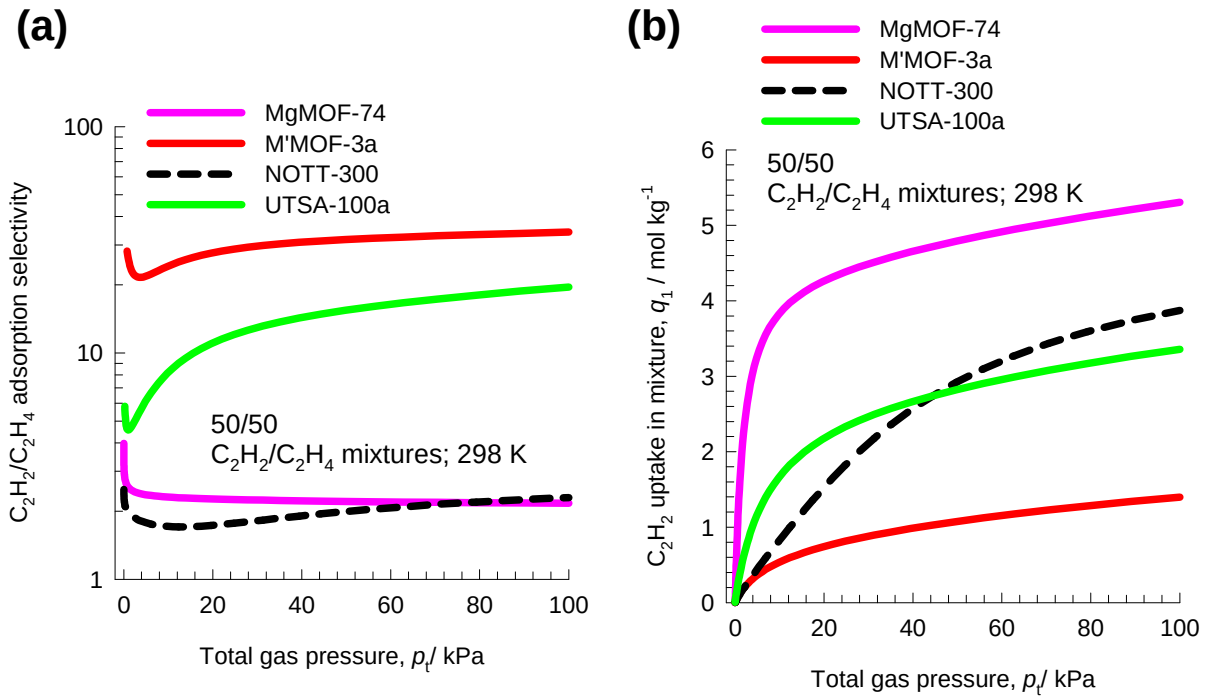

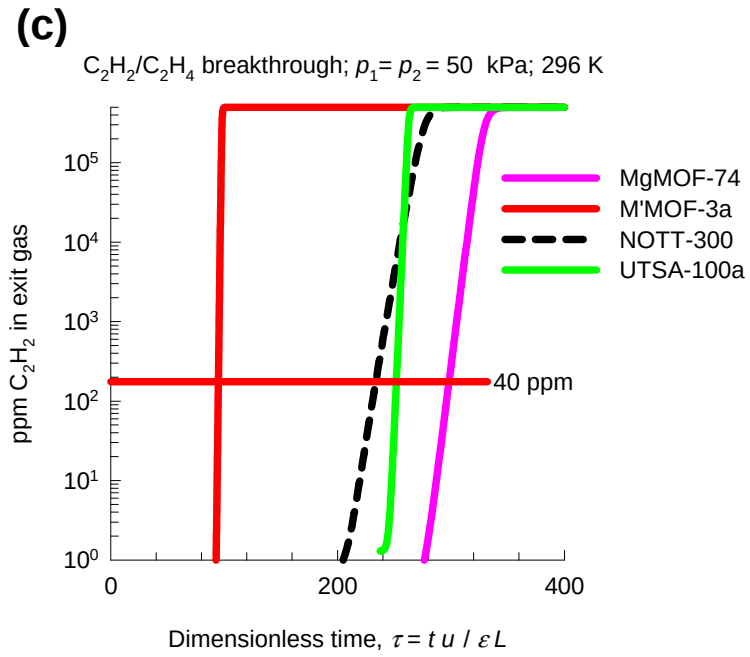

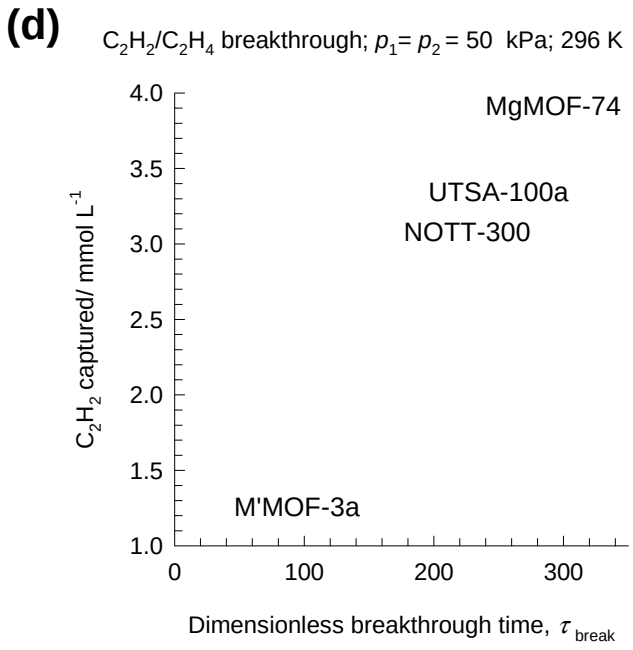

ESI Figure 11

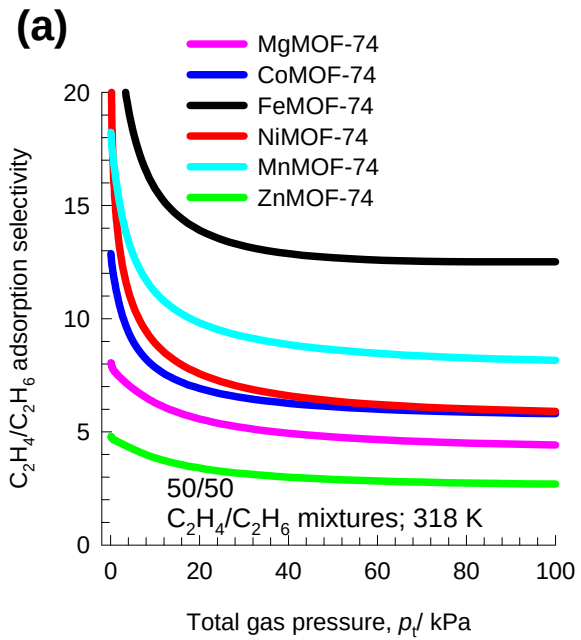

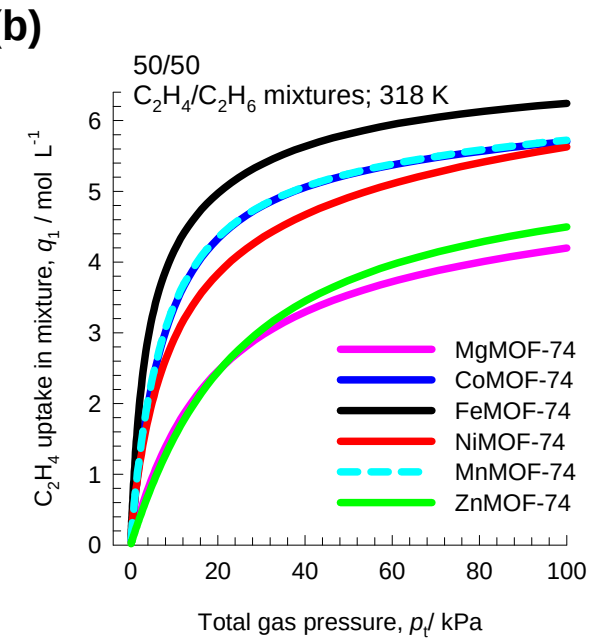

C_2H_4/C_2H_6 separations for 50/50 mixtures

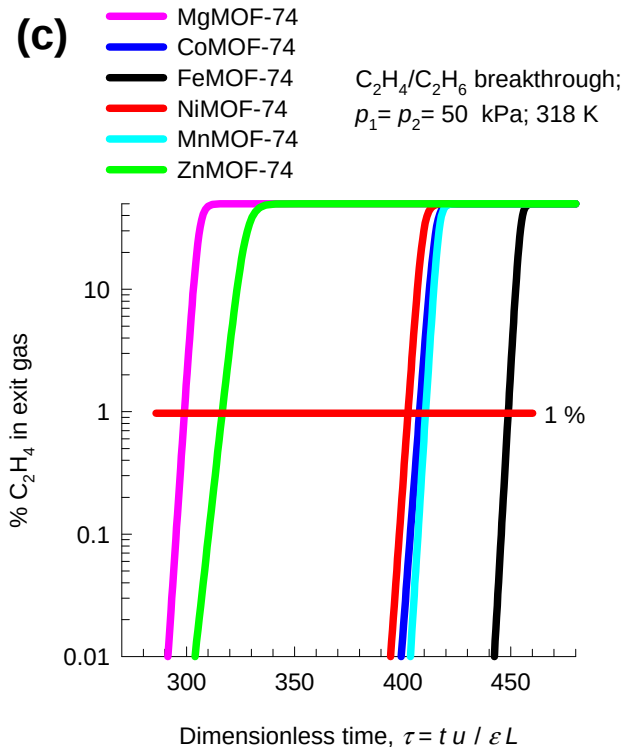

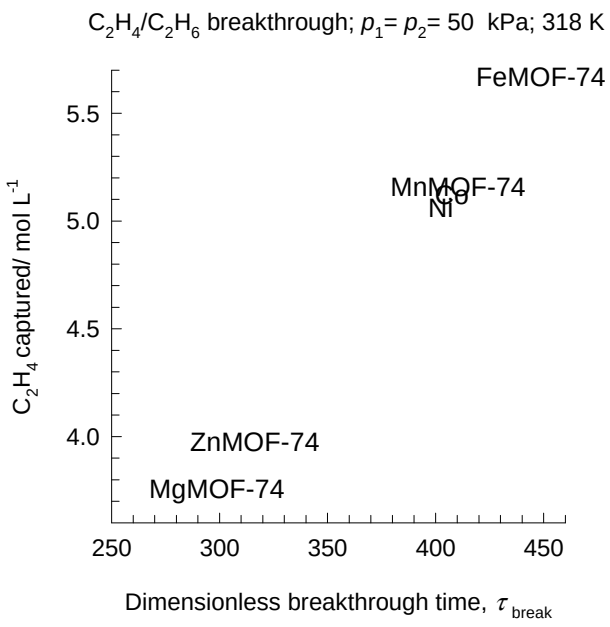

ESI Figure 12

C_3H_6/C_3H_8 separations for 50/50 mixtures

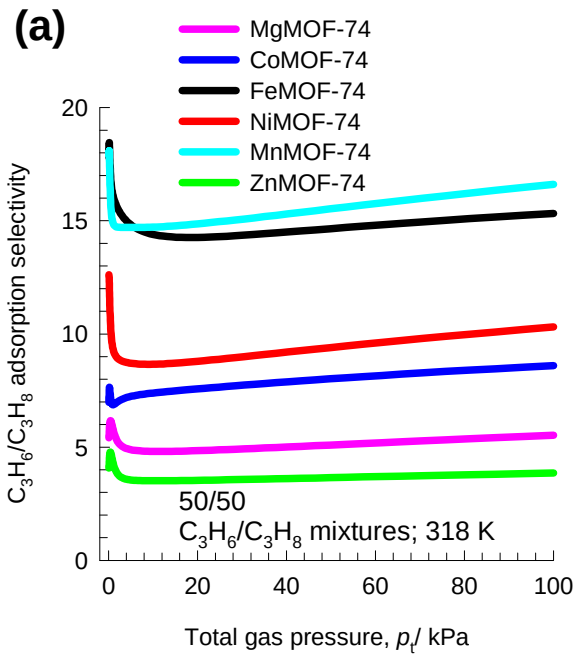

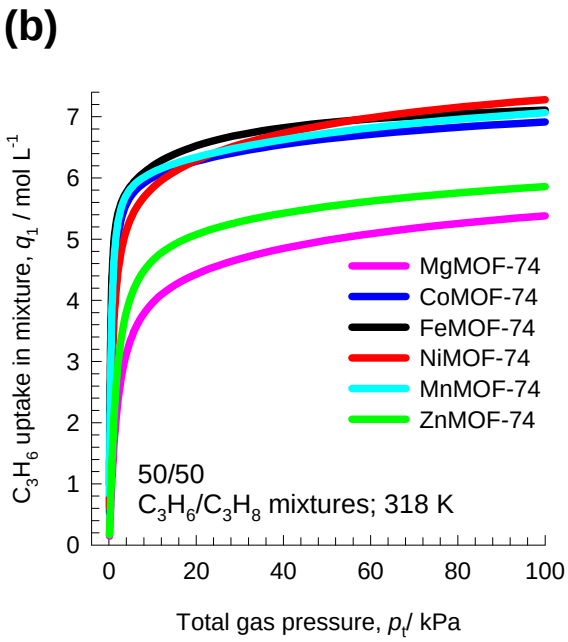

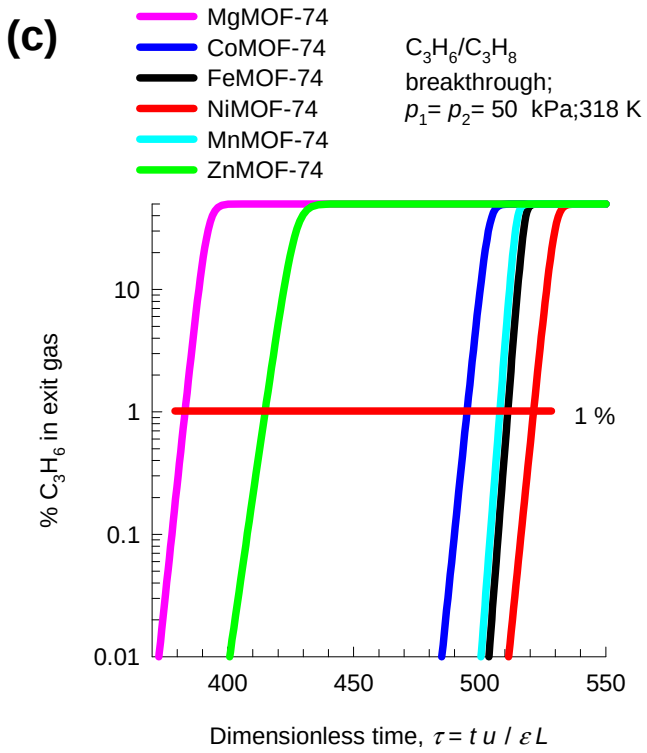

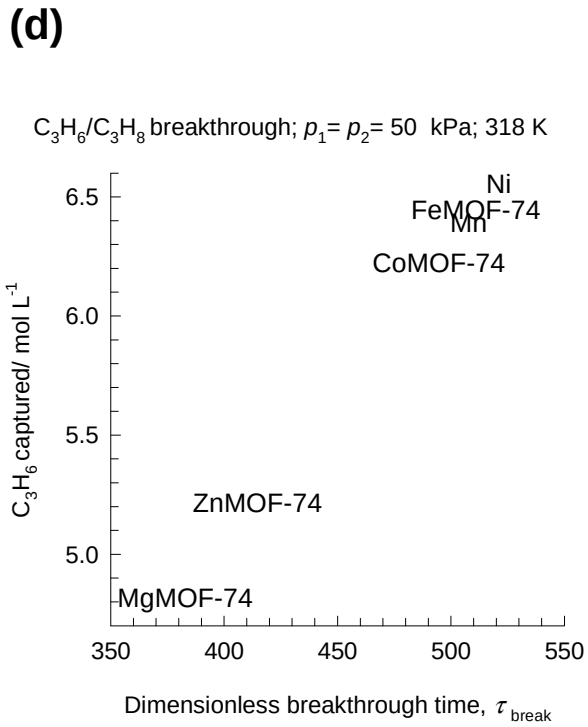

ESI Figure 13

Isosteric heats of adsorption for alkene/MOFs

(a)

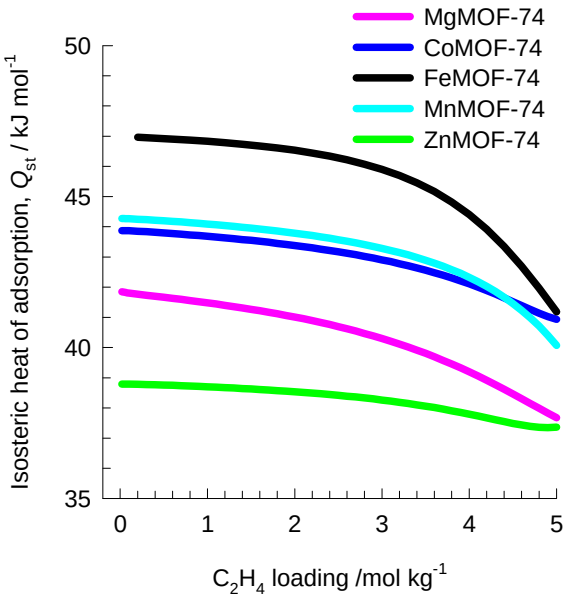

(b)

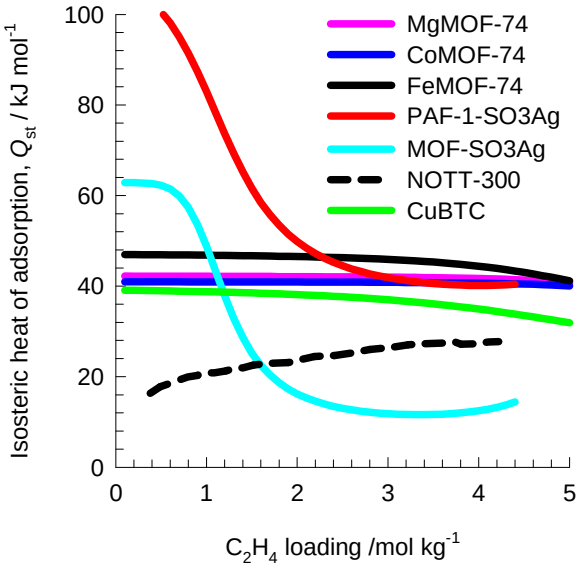

(c)

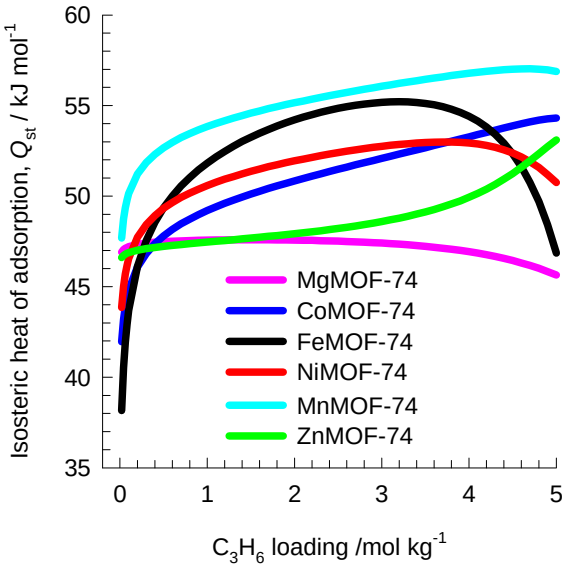

ESI Figure 14

Separations for hexane isomers

(a)

nC6-2MP-3MP-
22DMB-23DMB mixture;
Fe2(BDP)3; 433 K;
$f_1=f_2=f_3=f_4=f_5$ = 20 kPa;
with diffusion

(D_{nC6}/r_c^2) = 0.002 s^{-1}
(D_{nC6}/D_{2MP}) = 5
(D_{nC6}/D_{3MP}) = 5
(D_{nC6}/D_{22DMB}) = 10
(D_{nC6}/D_{23DMB}) = 10

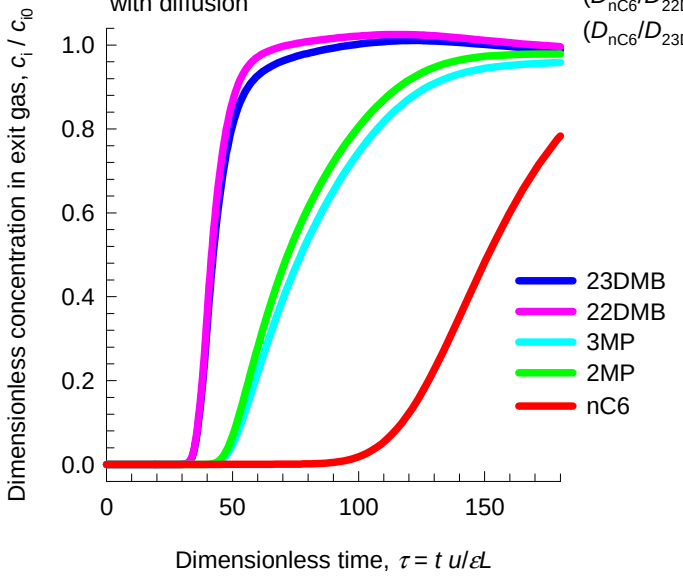

(b)

nC6-2MP-3MP-
22DMB-23DMB mixture;
ZIF-77; 433 K;
$f_1=f_2=f_3=f_4=f_5$ = 20 kPa

(D_{nC6}/r_c^2) = 0.0004 s^{-1}
(D_{nC6}/D_{2MP}) = 5
(D_{nC6}/D_{3MP}) = 5
(D_{nC6}/D_{22DMB}) = 10
(D_{nC6}/D_{23DMB}) = 10

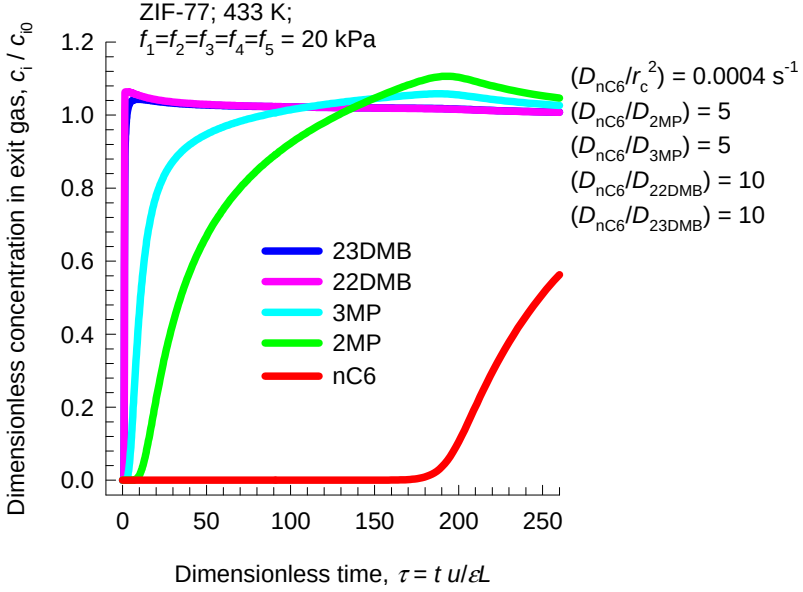

(c)

nC6-2MP-3MP-
22DMB-23DMB mixture;
MFI; 433 K;
$f_1=f_2=f_3=f_4=f_5$ = 20 kPa;
Including diffusion;
with thermo coupling

Dimensionless time, $\tau = t\,u/\varepsilon L$
(D_{nC6}/r_c^2) = 0.002 s^{-1};
(D_{nC6}/D_{2MP}) = 5
(D_{nC6}/D_{3MP}) = 5
(D_{nC6}/D_{22DMB}) = 25
(D_{nC6}/D_{23DMB}) = 25

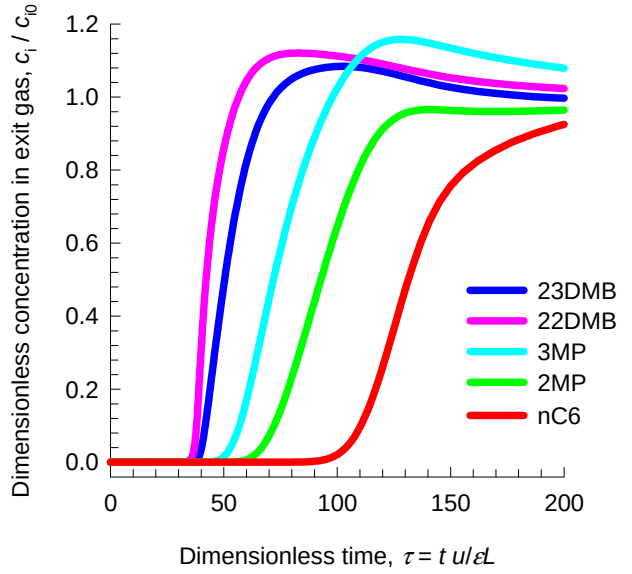

ESI Figure 15

Benzene, Cylcohexane structures

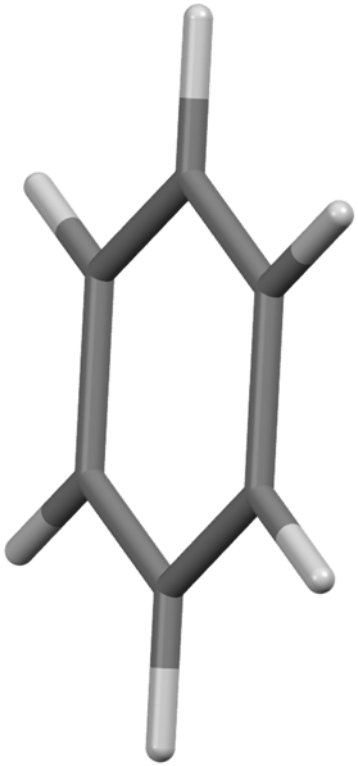

benzene

b.p.= 353.3 K

f.p. = 278.7 K

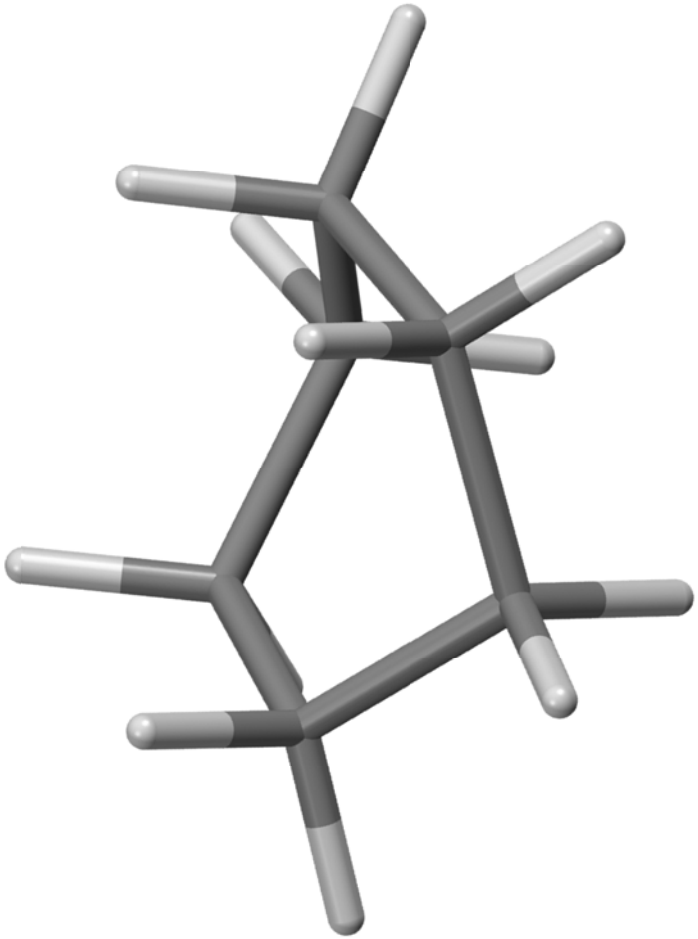

Cyclohexane boat

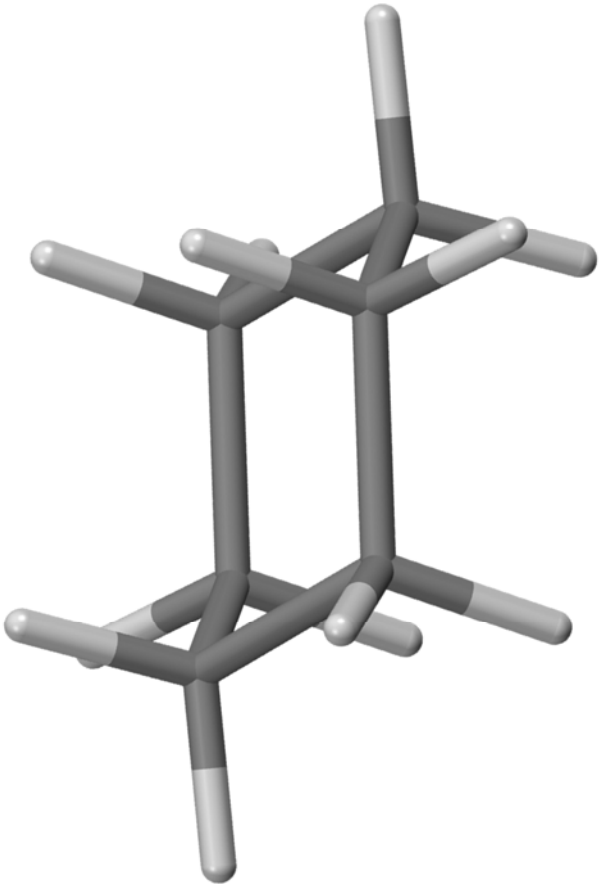

Cyclohexane chair

b.p.= 353.9 K

f.p. = 279.6 K

Benzene/Cylcohexane separations

(a)

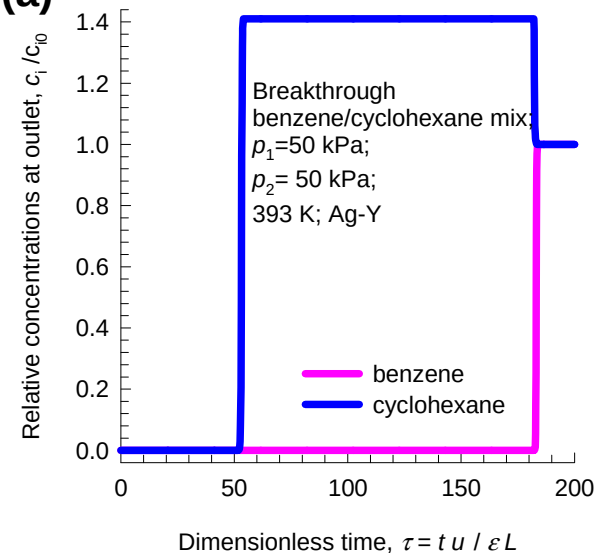

(b)

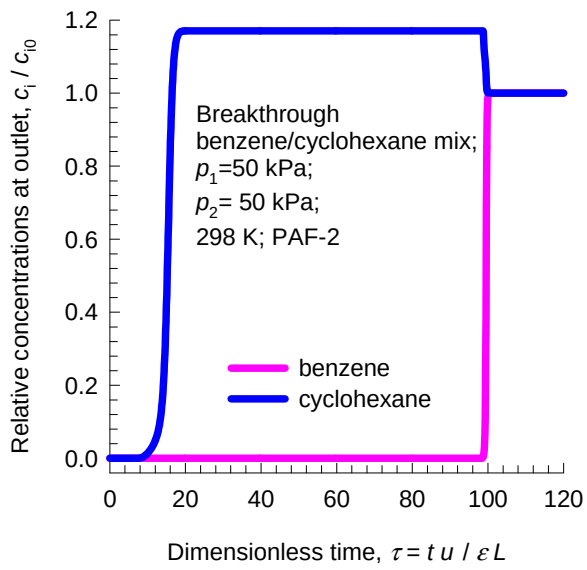

(c)